

Contents lists available at ScienceDirect

Dynamics of Atmospheres and Oceans

journal homepage: www.elsevier.com/locate/dynatmoce





Atmospheric forcing of the Hatteras coastal ocean during 2017–2018: The PEACH program

John Bane a, Harvey Seim A, Sara Haines Lu Han A, Ruoying He , Joseph Zambon B

- * University of North Carolina, Chapel Hill, NC, USA
- b North Carolina State University, Raleigh, NC, USA

ARTICLEINFO

Keywords:
Atmospheric forcing
Gape Hatteras
PEACH
Atmospheric cyclones
Atmospheric warm and cool seasons

ABSTRACT

The Hatteras coastal ocean is centrally located along the east coast of the 48 contiguous United States, offshore of Cape Hatteras in a complex land/ocean/atmosphere region where major ocean currents of differing temperatures and salinities meet and interact, where the atmosphere fluctuates on a wide range of time scales, and where atmosphere-ocean interactions vary both spatially and temporally. The Gulf Stream current typically leaves its contact with the continental margin here. Continental shelf currents from the north and from the south converge here, resulting in a net shelfto-ocean transport of shelf waters that carry important water properties and constituents. The two major drivers of these shelf currents and exchanges are the atmosphere and the oceanic Gulf Stream. Atmospheric driving of the Hatteras coastal ocean is through surface wind stress and heat flux across the air-sea interface. The complexity and importance of this region motivated the NSF-sponsored PEACH research program during 2017-2018 (PEACH: Processes driving Exchange At Cape Hatteras). In this paper, we utilize the substantial number of observations available during PEACH to describe the atmospheric forcing of the ocean then. Atmospheric conditions are described in terms of two seasons: the warm season (May to mid-September), with predominantly mild northeastward winds punctuated by occasional tropical cyclones (TCs); and the cool season (mid-September through April), with a nearly continuous, northeastward progression of energetic extratropical cyclones (ETCs) through the region. Cool season ETCs force the region with strong wind stress and ocean-to-atmosphere heat flux episodes, each with a time-scale of several days. Wind stress fluctuation magnitudes typically exceed mean stress magnitudes in each season by a factor of 3-5. These stresses account for just over 40% of the total current variability in the region, showing the wind to be a major driver of the ocean here. Atmosphere-ocean heat flux is typically into the ocean throughout the warm season (\sim 100 W m $^{-2}$); it is essentially always out of the ocean during the cool season (\sim 500 W m $^{-2}$ or more). New results herein include: southward intraseasonal oscillations of the jet stream's position drove the strongest ETCs (including one "bomb" cyclone); and during the 41 years leading up to and including PEACH, the season-averaged number and strength of atmospheric cyclones passing over the Hatteras coastal ocean have shown little long-term change. Looking ahead, the NSF Pioneer Array is scheduled to be relocated to the northern portion of the Hatteras coastal ocean in 2024, and the NASA SWOT satellite has begun its ocean topography mission, which has a ground-track cross-over here.

E-mail address: bane@unc.edu (J. Bane).

^{*} Correspondence to: Department of Earth, Marine & Environmental Sciences, University of North Carolina, Venable Hall - CB#3300, Chapel Hill, NC 27599-3300, USA.

1. Introduction

The Hatteras coastal ocean (33–37°N and out to ~200 km from shore; Fig. 1) is centrally located along the east coast of the 48 contiguous United States (Fig. 1 inset). It is offshore of Cape Hatteras in a complex land/ocean/atmosphere region where major ocean currents of differing temperatures and salinities meet and interact, where the atmosphere fluctuates on a wide range of time scales, and where atmosphere-ocean interactions vary both spatially and temporally. This is where the North Atlantic Ocean's subpolar and subtropical gyres meet and interact. This is also where the generally equatorward continental shelf currents along the Mid-Atlantic Bight (MAB, to the north of Cape Hatteras) converge with the generally poleward continental shelf currents along the South Atlantic Bight (\$AB\$, to the south of Cape Hatteras). This convergence results in a net off-shelf transport of shelf waters to the adjacent open ocean (Savidge and Bane, 2001; Todd, 2020; Han et al., 2022), and it often produces a discernable sea surface temperature (\$ST) front on the shelf at the convergence, known as the Hatteras Front (Savidge, 2002; Savidge and Austin, 2007; see Fig. 1). Although net seawater transport is from the continental shelf to the open ocean, shelf-ocean water exchanges are spatially and temporally variable, and episodes of ocean-to-shelf transport also occur (Yoder et al., 1983; Lee et al., 1984, 1991; Todd, 2020; Muglia et al., 2020; Han et al., 2022). Important water properties (e.g., temperature, salinity and density), biological constituents and anthropogenic pollutants are advected by these exchanges (Yoder et al., 1983; Savidge, 2002; Han et al., 2021).

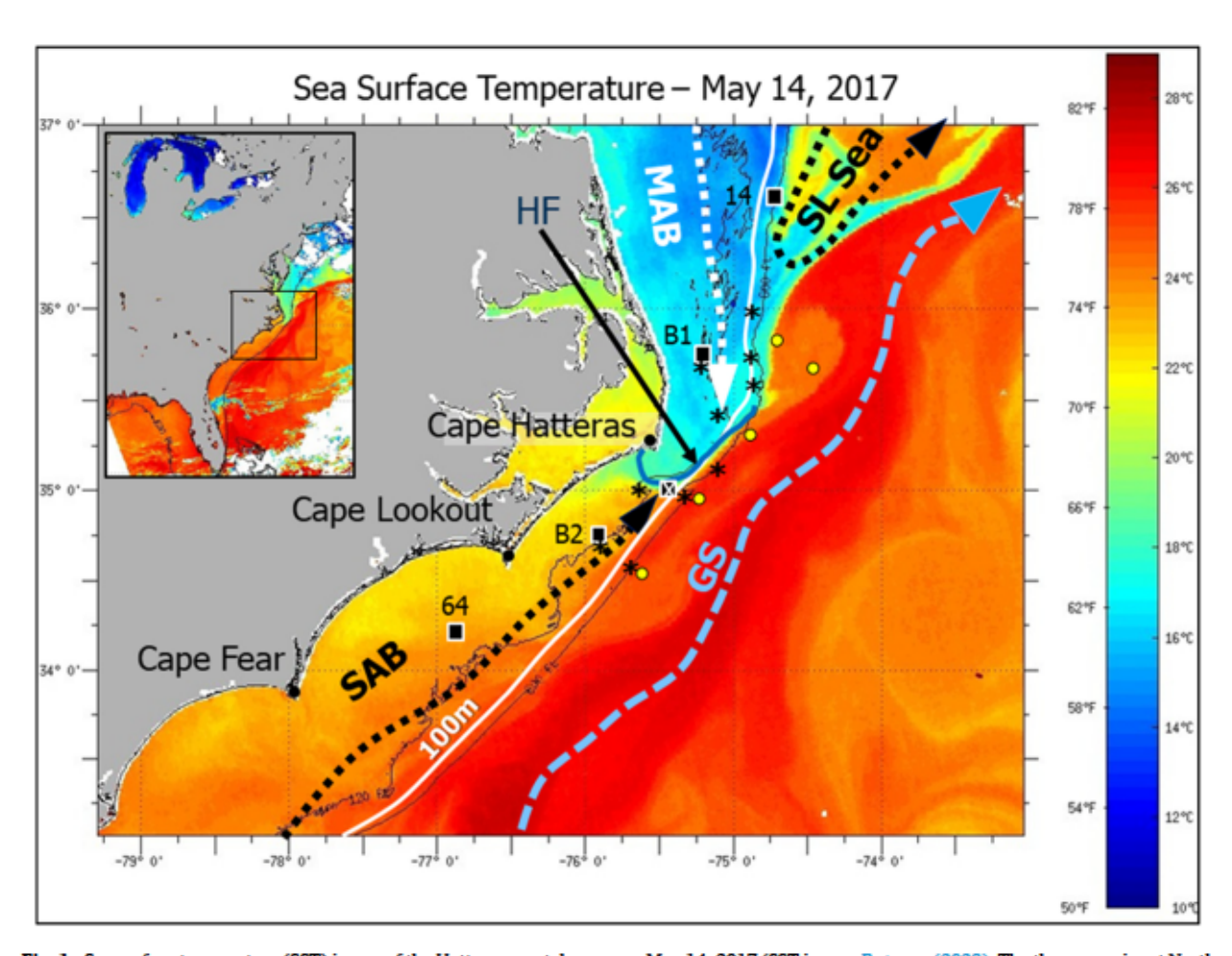


Fig. 1. Sea surface temperature (SST) image of the Hatteras coastal ocean on May 14, 2017 (SST image: Rutgers. (2023). The three prominent North Carolina Capes are denoted with dots. The positions of meteorological buoys and oceanographic moorings deployed during the PEACH field program (April 2017 through November 2018) are shown. The 100 m isobath (white line) delineates the continental shelf break. Over the continental shelf, the typically northeastward flowing SAB and southward flowing MAB shelf waters converge, forming the Hatteras Front (HF). Surface buoys (squares outlined in white) from north to south are 44014, B1 (w/co-located ocean ADCP and CTD, asterisk), 41025 (located on 35°N latitude; white x in square), B2 (w/co-located ocean ADCP and CTD, asterisk), and 41064. Additional ocean ADCP and CTD moorings from north-to-south are A1 through A8 (asterisks). Bottom-moored CPIES are yellow circles. Schematic shelf flows and surface flows in the Gulf Stream (GS) and Slope Sea (SL Sea) are also shown. [ADCP: Acoustic Doppler Current Profiler, which can remotely measure ocean currents throughout the water column; CTD: Conductivity-Temperature-Depth sensor, which determines ocean water temperature, salinity and pressure (depth) at the instrument's location; CPIES: Current-meter and Pressure-sensor equipped Inverted Echo Sounder, which can determine the Gulf Stream's lateral (onshore-off-shore) position.].

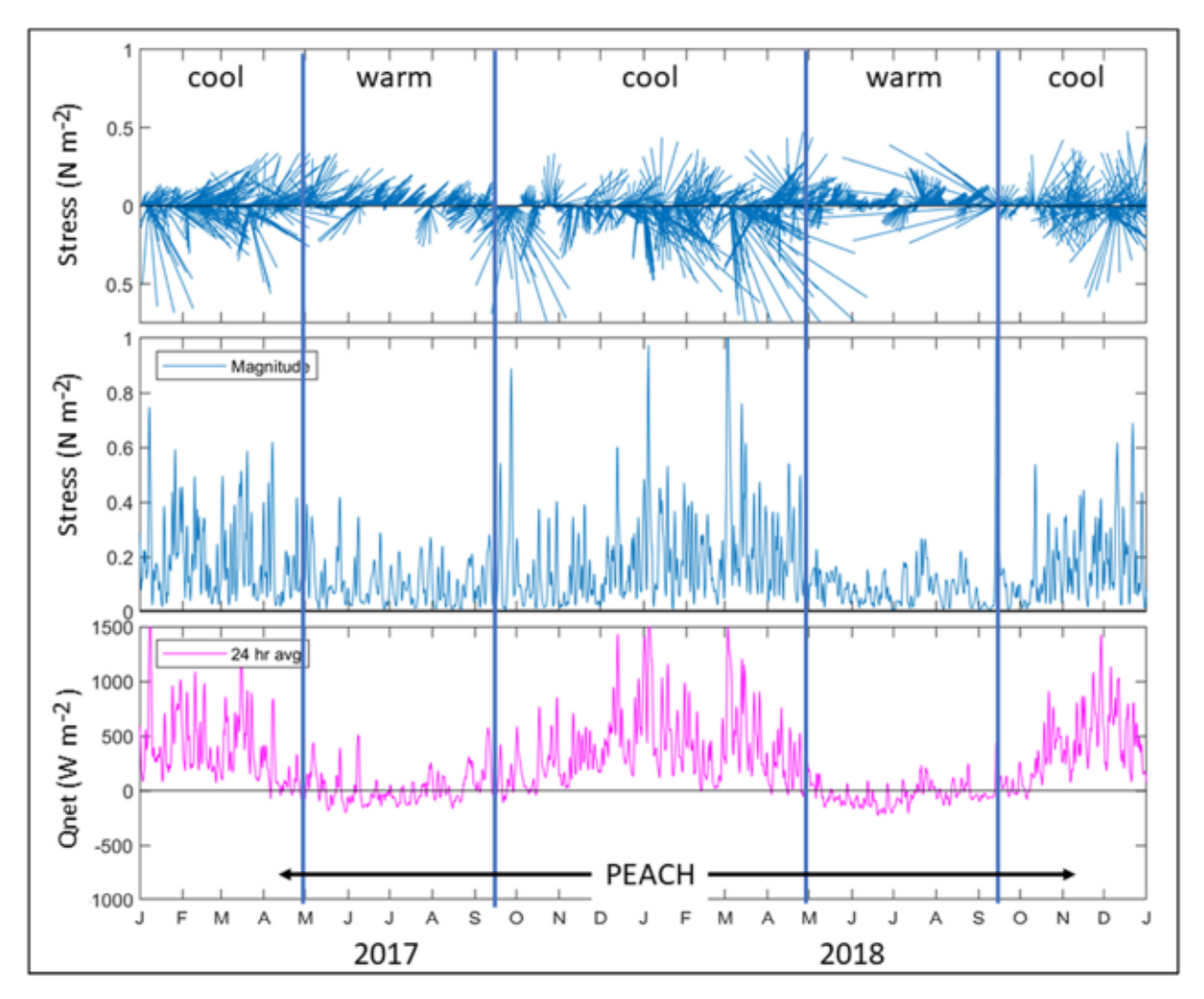


Fig. 2. Time series at the location of Buoy 41025, computed from ERA5 data. These show the two-season character of wind stress (top, middle) and net ocean-to-atmosphere heat flux across the air-sea interface (Q_{net} ; bottom) during 2017–18, which encompasses the PEACH field program. The wind stress stick-vectors (top) point from the horizontal axis towards the direction the wind was blowing. Q_{net} is the sum of: long-wave infrared radiation arriving at and emitted from the sea surface, short-wave solar radiation across the sea surface, latent (evaporative) heat flux from the ocean surface, and sensible (conductive) heat flux between the atmosphere and ocean across the sea surface: $Q_{net} = Q_{LWnet} - Q_{SWnet} + Q_{lat} + Q_{sen}$ (see also Pinker et al., 2014). Each heat flux component is considered positive when the heat is transferred from the ocean to the atmosphere.

The two major drivers of these shelf currents and shelf-ocean exchanges are the atmosphere, through surface wind stress and heat flux across the air-sea interface, and the meandering Gulf Stream, which flows poleward along the continental slope of the SAB from the Florida Straits to and through the Hatteras coastal ocean before leaving the slope to continue into the open North Atlantic (Fig. 1). Bach driver is spatially and temporally variable. The early study by Savidge and Bane (2001) found that along-shelf seawater volume transport variability was primarily wind-driven, while along-shelf seawater transport convergence was highly correlated with Gulf Stream lateral position offshore. These findings provided motivation for the National Science Foundation-sponsored PEACH research program during 2017–2018 (PEACH: Processes driving Exchange At Cape Hatteras), which has deepened our understanding of these two major driving factors and the oceanic responses to them. Seim et al. (2022) provide a more complete overview of the PEACH program and initial results.

The objectives of this paper are two-fold: 1) As a contribution to the PEACH research program, we document and describe the atmosphere and its forcing of the Hatteras coastal ocean; and 2) We demonstrate that the atmospheric mean conditions and variability can be described in a 2-season manner, which is essentially a new view of this region. Using observed atmospheric and oceanic data, Coastwatch SST data (Li et al., 2001), and ERA5 reanalysis data (ECMWF Re-Analysis, 5th Generation; Hersbach et al., 2018), we describe the atmosphere and atmosphere-ocean interactions in the Hatteras coastal ocean during 2017–2018, a period encompassing the PEACH field program (April 2017 through November 2018). Based on inspection of the time series of surface wind stress and ocean-to-atmosphere heat fluxes, our description is given in terms of the atmospheric "warm season" and atmospheric "cool season" (Fig. 2). During each warm season (May through mid-September), prevailing mild northeastward winds (southwesterly winds in the

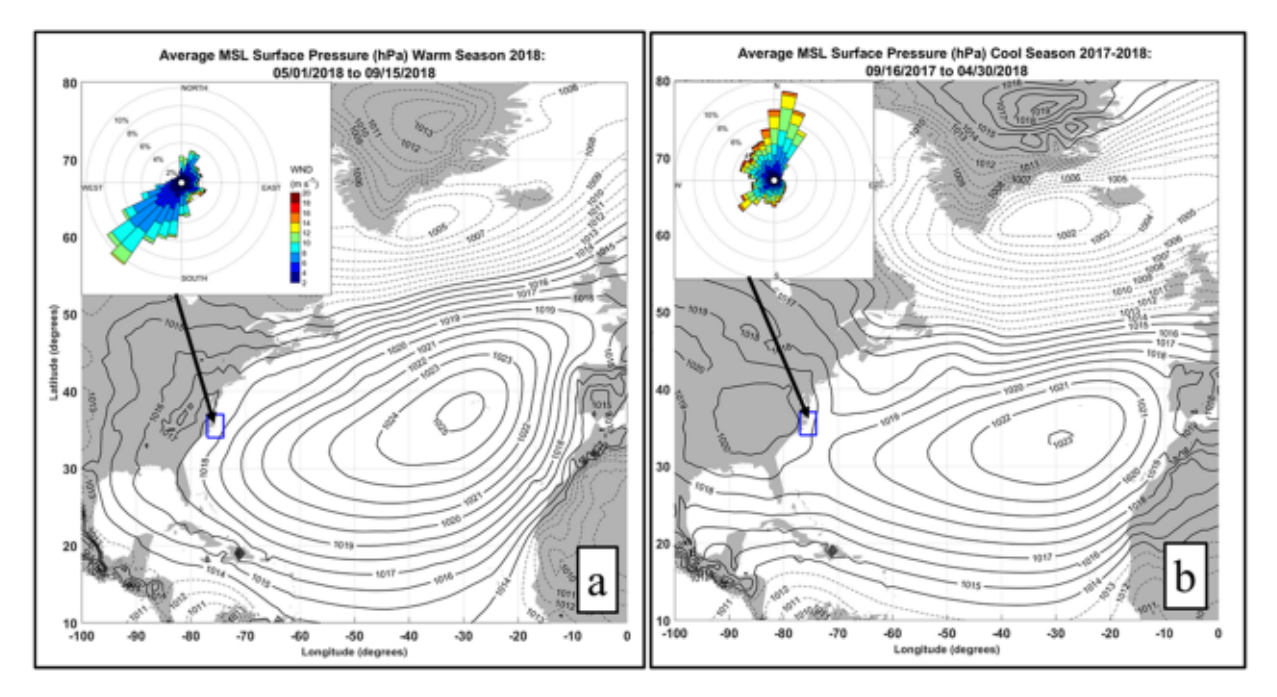


Fig. 3. The mean surface atmospheric pressure distribution during (a) the 2018 warm season, and (b) the 2017–18 cool season, based on ERA5 reanalysis data (Hersbach et al., 2018). The Hatteras coastal ocean is outlined by the rectangle. The wind velocity rose from Buoy 41025 is shown for each season (inset, in which the meteorological convention is used for direction; i.e. the bars point towards the direction the wind is coming from). Mild northeastward (southwesterly) winds were typical in the warm season, and strong southward (northerly) winds were common in the cool season.

meteorological convention) were affected occasionally by the passage of a weak extratropical cyclone (ETC), causing slight variations in wind strength and direction. Additionally, the 2017 warm season at PEACH was impacted by one hurricane, and the 2018 warm season received forcing from two hurricanes. During each cool season (mid-September through April), there was a nearly continuous northeastward progression of moderate to strong ETCs through PEACH, including one "bomb" cyclone. Two hurricanes affected PEACH during the 2017–18 cool season, and one during the 2018–19 cool season. Herein we take May 1 and September 16 as the beginning dates for the warm and cool seasons, respectively.

2. Observations and methods

Three NDBC meteorological buoys (44014, 41025, 41064; NDBC = National Data Buoy Center, noaa.ndbc.gov) were in place during all of 2017 and 2018, and the two PEACH meteorological buoys (B1, B2) were deployed in the study area for the duration of the field program (Fig. 1). Two warm seasons and one full and two partial cool seasons were measured by the complete buoy array during PEACH. In Fig. 2 wind stress vectors are plotted as "sticks" which point from the time axis and towards the direction the wind was blowing (oriented with true north up). Herein we take positive heat flux to be across the air-sea interface and from the ocean to the atmosphere. Buoys B1 and B2 carried meteorological sensors (wind speed and direction, air temperature, humidity, barometric pressure, downwelled short- and long-wave.

radiation and precipitation), and near-surface and mid-depth CTDs, all of which sampled every 6 min. Surface observations from NDBC buoys provided wind speed and direction, air temperature, humidity, barometric pressure, SST, and wave dynamics (height, speed, and direction) every hour. Sufficient input variables and coverage allowed for computing hourly estimates of the primary heat flux components using COARE 3.6 algorithms (Edson et al., 2013). In the Appendix, we describe in detail the data processing steps necessary to compute wind stress and bulk heat flux from buoy measurements at each of the five buoy locations.

In-ocean instruments were moored over the continental shelf and slope (Andres, 2021; Han et al., 2021, 2022; Seim et al., 2022) and beneath the Gulf Stream (Andres, 2021) to measure currents and hydrographic properties (Fig. 1). Time-series of horizontal water velocity profiles and bottom water properties (temperature, salinity, density, and pressure) were sampled every 30 min from bottom-mounted ADCPs at four mid-shelf locations (B1, B2, A4, A7) and six shelf break locations (A1, A2, A3, A5, A6, A8). The lateral position of the Gulf Stream jet was measured with bottom mounted CPIES. [Instrument acronyms are: ADCP = Acoustic Doppler Current Profiler, which can remotely measure ocean currents throughout the water column; CTD = Conductivity-Temperature-Depth sensor, which determines ocean water temperature, salinity and pressure (depth) at the instrument's location; CPIES: Current-meter and Pressure-sensor equipped Inverted Echo Sounder, which measures the depth of the oceanic permanent thermocline, and thereby locates the position of the meandering Gulf Stream.].

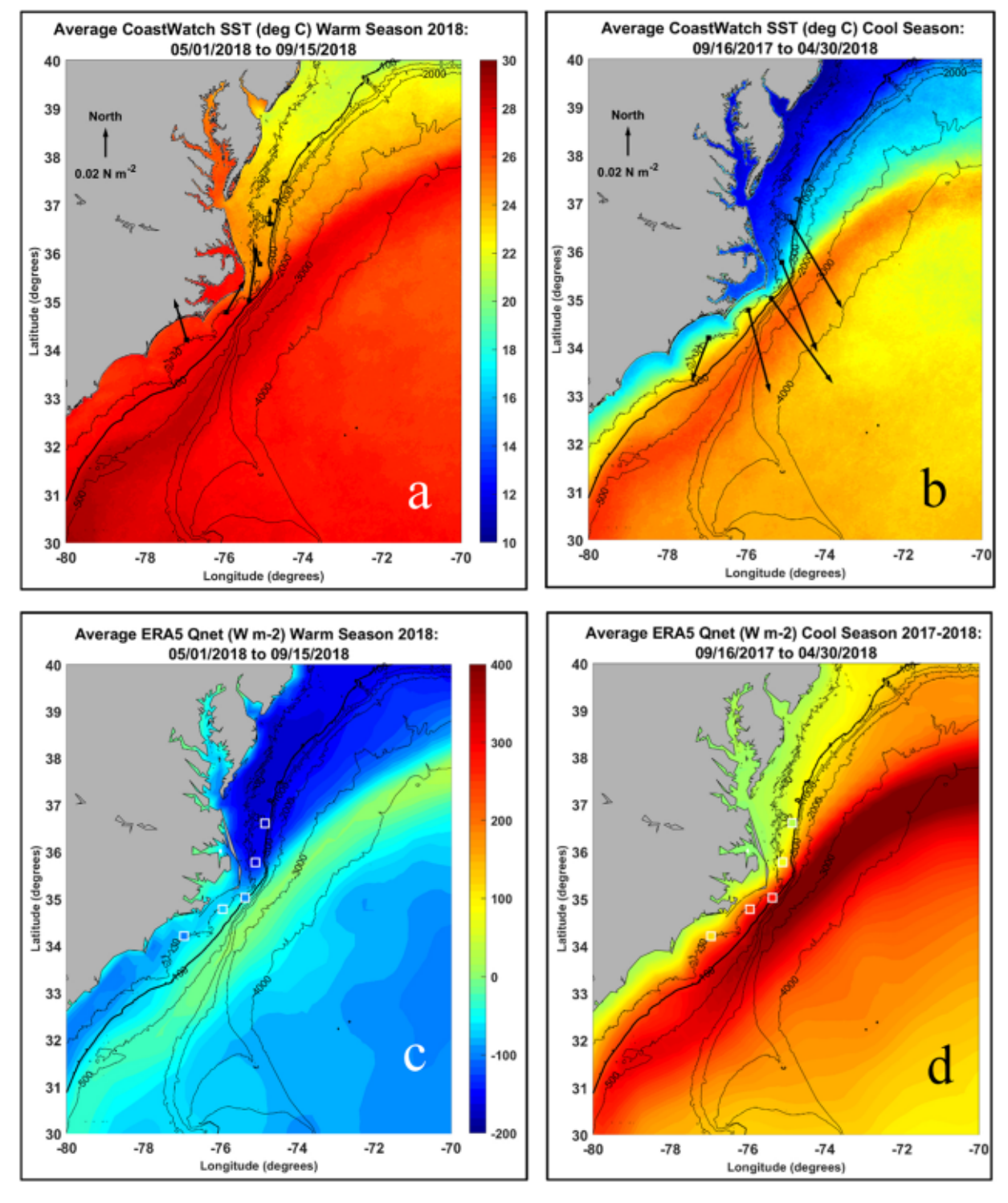
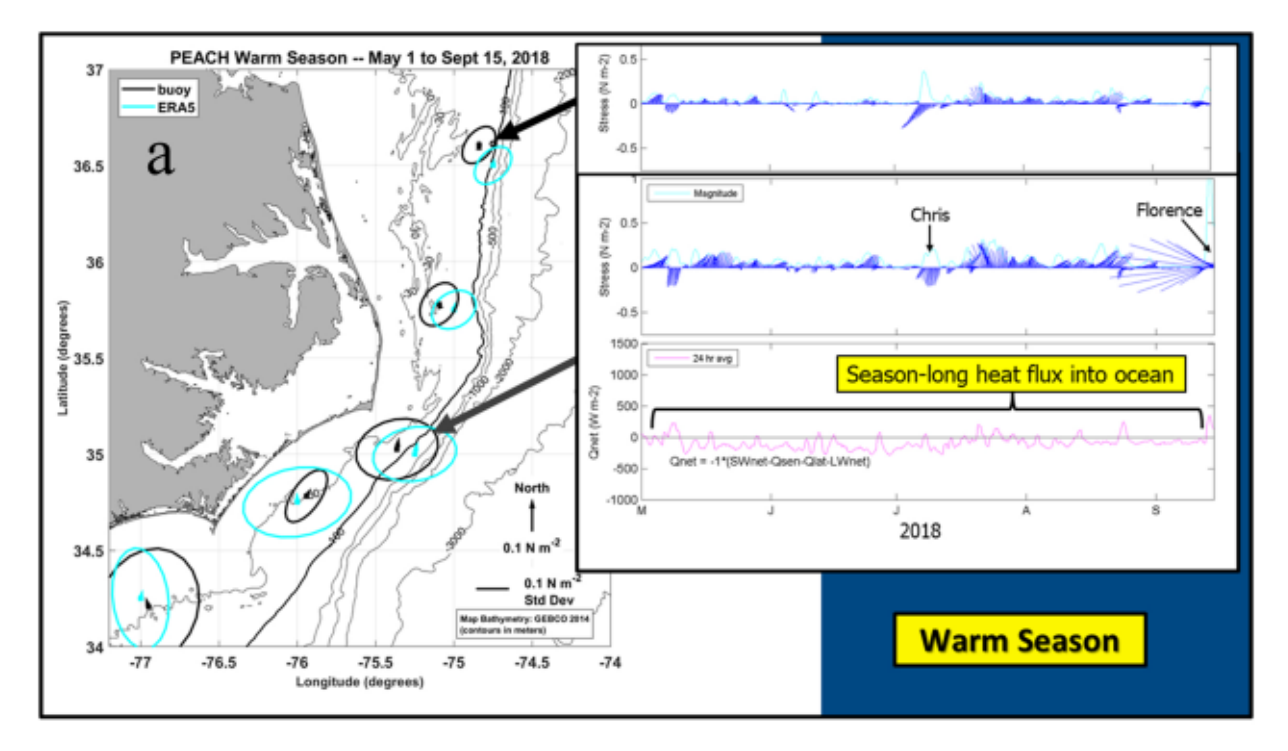


Fig. 4. The average Coastwatch SST during (a) the 2018 warm season and (b) the 2017–18 cool season. The season-average wind stress observed at each buoy is shown for each season. The net ocean-to-atmosphere heat flux, $Q_{\rm net}$, during (c) the 2018 warm season and (d) the 2017–18 cool season from ERA5. For comparison, the average $Q_{\rm net}$ measured at each buoy is shown for each season (squares). Isobaths are in meters, and the 100 m isobath is bold.



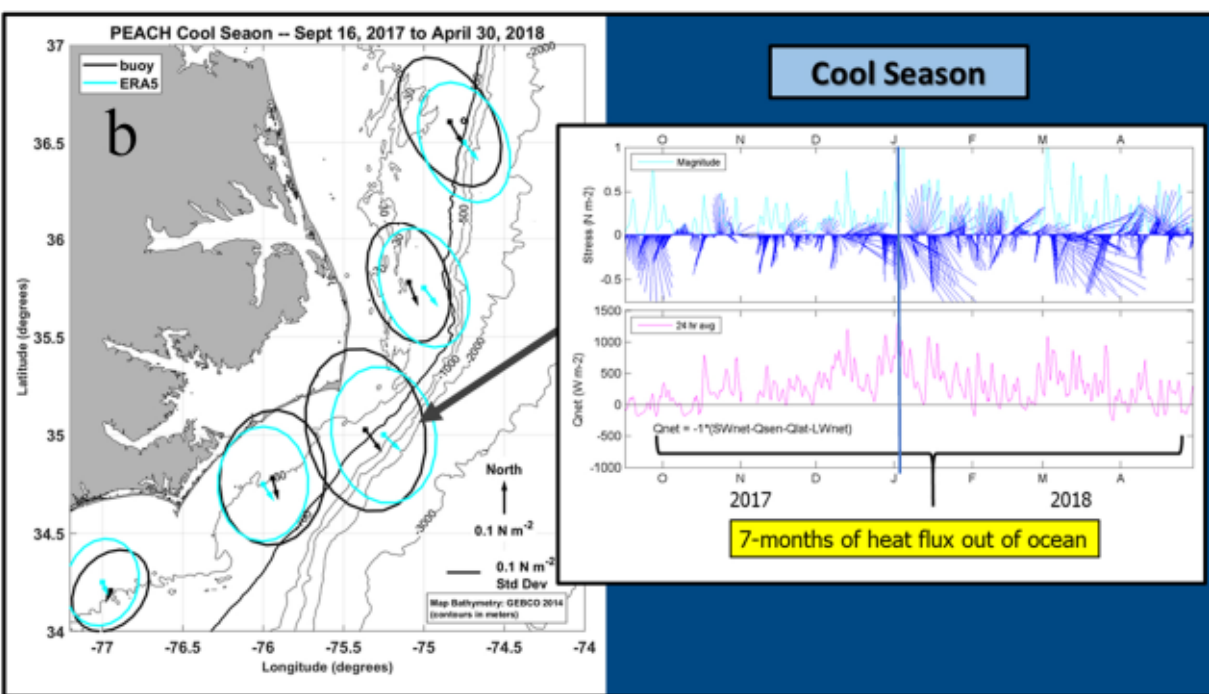


Fig. 5. Wind stress and Q_{net} for (a) the 2018 warm season and (b) the 2017–18 cool season. On the left, arrows and standard deviation ellipses in black are from buoy observations; those in cyan are from ERA5. Here the mean stress arrows and the std ellipses are plotted on the same scale (different from the stress scale in Fig. 4). The stress variations in either season are typically several times greater than the mean stress at each location. Vertical line in (b) is "bomb" cyclone Grayson.

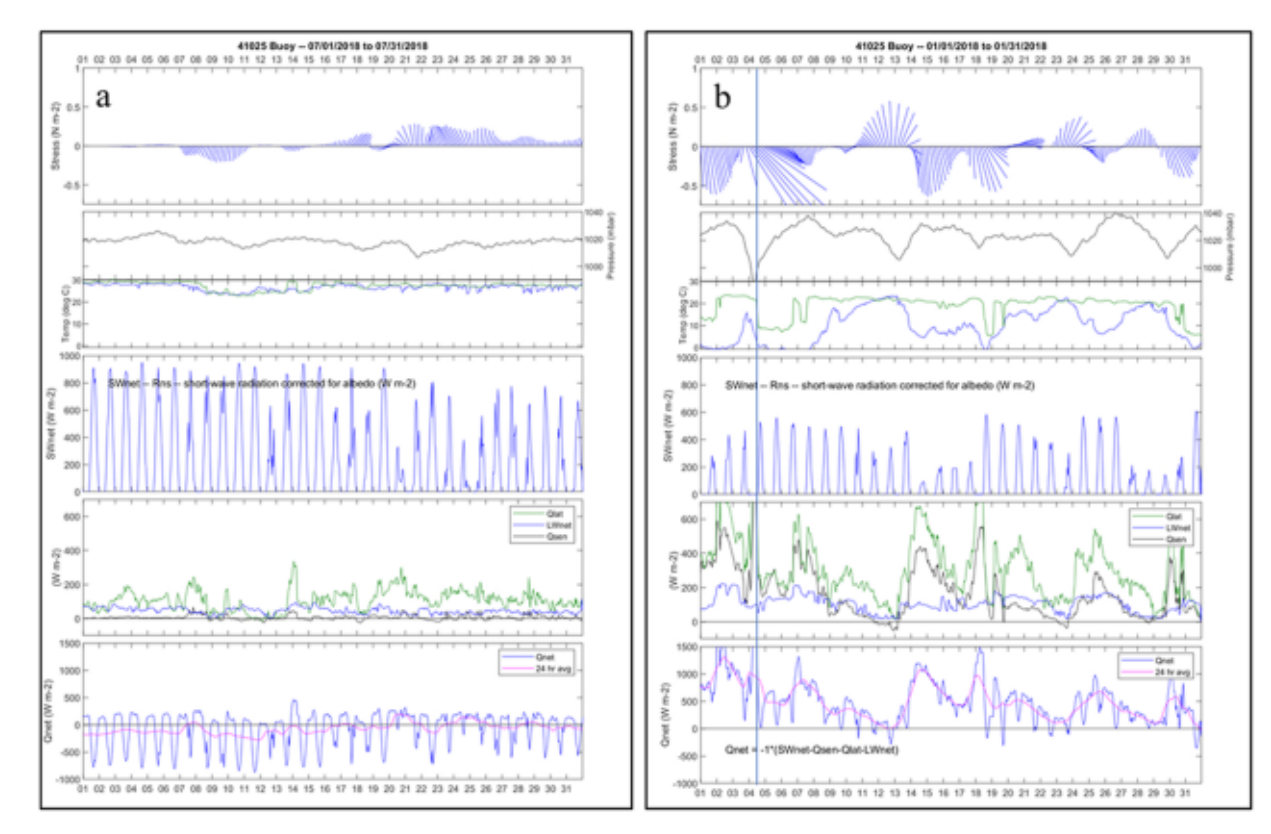


Fig. 6. Time series from Buoy 41025 showing (a) a typical warm season month (July 2018) and (b) a typical cool season month (January 2018). From top to bottom: wind stress (true north is up); surface air pressure; near-surface air temperature (blue) and near-surface ocean temperature (green); net shortwave radiation; ocean-to-atmosphere heat flux components (latent, green; sensible, blue; and longwave, cyan); hourly and 24-hravg Q_{net}. The vertical line in January is the time of the weather map in Fig. 9 below, when bomb cyclone Grayson was passing this buoy.and 6b. This was winter cyclone Grayson, described in more detail below. This ETC developed rapidly enough [3.3 Bergeron (about 50 hPa) in 24 h at 33°N latitude] to be considered an explosive cyclone, or "bomb" cyclone (Hirata et al., 2019).

3. The atmospheric warm and cool seasons

3.1. Warm and cool season mean conditions

In the long-term mean, the western periphery of the semi-permanent North Atlantic subtropical high pressure cell (the North Atlantic High, sometimes called the Azores High or the Bermuda High) overlies the Hatteras coastal ocean and thus the PEACH instrumentation array. The extent and strength of this cell varies on an annual basis (Davis et al., 1997, who describe a mean "summer pattern" and a mean "winter pattern" similar to our warm and cool seasons) and on longer time scales (Li et al., 2012, 2013). During 2017-18, the major atmospheric variation through an annual time frame was the transition from a cool season (mid-September through April) to a warm season (May to mid-September) and back again. One effect of this transition on the PEACH region can be seen in the seasonal mean atmospheric surface pressure patterns in Fig. 3. During the warm season, PEACH is within the North Atlantic High, and mean geostrophic winds are thus northeastward (wind speed rose in Fig. 3a, and mean wind stress arrows in Figs. 4a, 5a), while in the cool season, PEACH is within a smaller scale continental high pressure area, and mean geostrophic winds are generally southward (wind speed rose in Fig. 3 b, mean wind stress arrows in Figs. 4b, 5b). This cool season continental high is due in part to the numerous low-pressure-center ETCs that transit northeastward along the Eastern Seaboard of North America (which we describe in more detail below), thereby enhancing a seasonal-average surface-low-pressure trough through the western end of the North Atlantic High that stretches from Florida to Newfoundland. Interannual and longer term variations in the North Atlantic High are typically reflected in the North Atlantic Oscillation Index (NAO Index; Hurrell et al., 2003; Benedict et al., 2004; Li et al., 2013). During the 2017 (2018) warm season, the NAO Index was around - 0.5 (1.7) (NOAA., 2022a). During the 2016-17 (2017-18, 2018-19) cool season, the NAO Index was around 0.7 (0.5, 0.7). Additional details on the NAO variability are presented below.

The average SST field during each season is shown in Fig. 4 (SST data from Coastwatch: NOAA., 2022b). The warm Gulf Stream is apparent in each panel, and the cooler surface waters over the MAB and Slope Sea (Csanady and Hamilton, 1988) are apparent in both seasons. The surface warming during the warm season makes the SST contrast between the MAB and Slope Sea and the Gulf Stream less striking then, as compared to the cool season. In the SAB, the seasonal SST contrast between the Gulf Stream and the continental shelf & upper-slope is quite low during the warm season, and is greater in the cool season, primarily due to the lower SST inshore of the

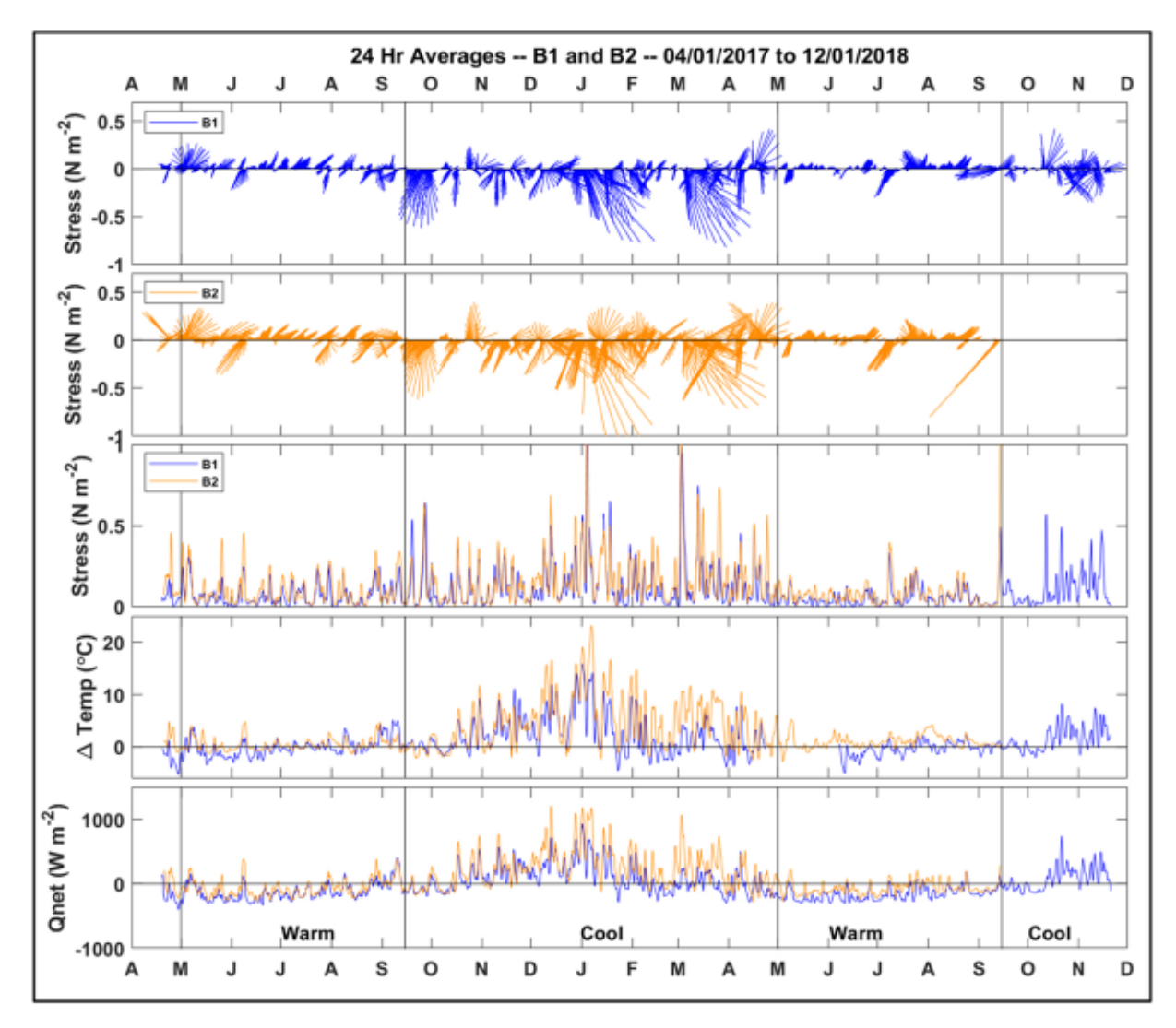


Fig. 7. Time series from Buoys B1 (north of Cape Hatteras on the southern MAB shelf) and B2 (south of Cape Hatteras on the northern SAB shelf, see Fig. 1) during PEACH. The clear coherence between the pairs of time series is due to the large lateral scale of the atmospheric systems, mostly ETCs, in comparison to the separation distance between these 2 buoys. Δ Temp is sea-temperature (2 m below surface) minus air-temperature (1.5 m above the surface).

Stream then. The lower cool season SST inshore of the Stream is due primarily to loss of heat from the shallow waters to the atmosphere (Atkinson et al., 1983, 1989).

During the 2018 warm season, the mean wind stress was generally poleward at each buoy, at around 0.01–0.02 N m⁻² (Figs. 4a, 5a). The stress standard deviation (std) was several times the mean stress at each location, and the orientation of each std ellipse major axis was close to NE-SW (Fig. 5a). An important aspect of the stress distribution is that mean and std values at the two locations north of Cape Hatteras were consistently lower than those south of the Cape. This is primarily an SST effect due to the MAB shelf flow bringing cooler waters to the Hatteras coastal ocean from the north, which results in relatively stable near-surface atmospheric conditions much of the time north of the Hatteras Front (Schutt and Seim, 2020; Thomas et al., 2015). Note the cooler SST north of the Hatteras Front in the "snapshot" in Fig. 1, for example. Additionally, localized coastal upwelling can occur around 36°N, when the winds are sufficiently strong in the northward direction, thereby decreasing the nearshore SST further and strengthening the lower atmospheric stability there (Austin and Lentz, 1999).

Ocean-to-atmosphere net heat flux ($Q_{net} = Q_{LWnet} - Q_{SWnet} + Q_{lat} + Q_{sen}$) was around -100 W m^{-2} (heat into the ocean) for nearly all of the 2018 warm season (Figs. 4c, 5a, 6). The typically warm and humid overlying air kept sensible and latent heat flux magnitudes low (\sim 100 W m $^{-2}$ out of the ocean) compared to cool season values, and strong solar irradiance dominated (\sim 100–200 W m $^{-2}$ typical daily average into the ocean). This resulted in a warming trend for much of the season. For reference, an average heat input rate of 100 W m $^{-2}$ into a water column of 30 m (\sim mid-shelf) would increase column-average water temperature about 1 0 C in 2 weeks.

During the 2017-18 cool season, the mean wind stress was southeastward at the northern four buoys, and southwestward at the

southernmost buoy. Season-long mean stresses were around 0.05 N m^{-2} (Figs. 4b, 5b). The temporal variability in wind stress was considerably larger than the mean stress at each buoy, due almost entirely to numerous ETCs and an occasional tropical cyclone (TC) progressing through the region. The stress std was around 0.2 N m^{-2} throughout the array, and several episodes of wind stress exceeding 0.5 N m^{-2} occurred (Fig. 2). The ocean-to-atmosphere Q_{net} varied both spatially and temporally. The season-long mean was several tens of W m $^{-2}$ over the shelf areas, and was about 300 W m $^{-2}$ over the Gulf Stream. Both areas experienced net heat flux out of the ocean (Figs. 4d, 5b). We note that the Hatteras coastal ocean is at the western end of the region of very high climatological Q_{net} in the North Atlantic, which basically follows the warm Gulf Stream northeastward from Hatteras to around 45°N ,

 40° W, and then extends poleward to both sides of Greenland (Yang et al., 2016; Schmitt, 2018). The long-term average Q_{net} in that swath ranges up to \sim 150 200 W m⁻² from the ocean, which is about midway between the warm and cool season values over the Gulf Stream in Fig. 4c,d.

3.2. Warm season variability

Typical warm season characteristics appear in the 2018 time series shown in Figs. 2, 5a and 6a: relatively weak wind stress, low airsea temperature difference, and low Q_{net} magnitudes. Wind stress was nearly always towards the northeast, varying with periodicities in the 3-to-10 day band (the typical time between successive ETC passages; also called the summer weather band) and with magnitudes reaching about $0.1 \, 0.2 \, \text{N m}^{-2}$. Focusing on July 2018 (Fig. 6a), the surface atmospheric pressure showed small fluctuations, associated with weak warm season ETCs progressing through. Wind stress pulses from two hurricanes (Chris and Florence) were recorded during the 2018 warm season (Fig. 5a). Cyclone tracks are discussed further below.

3.3. Cool season variability

Typical cool season characteristics are apparent in the 2017–18 time series shown in Figs. 2, 5b and 6b: continually fluctuating wind stress with stress episodes that often peaked at around 0.5 N m^{-2} (about 3–5 times stronger than those in the warm season), and episodes of large air-sea temperature differences and large Q_{net} magnitudes, frequently reaching 500–1500 W m⁻² from the ocean. Essentially all of these fluctuations were associated with ETC passages. An ETC passage occurred about every 3–7 days (the winter weather band), and each left a low-pressure signature at one or more of the buoys. Focusing in on January 2018, six low-pressure occurrences can be seen in Fig. 6b. Wind stress direction varied from generally poleward to generally equatorward as an ETC passed. The strongest wind stress episode measured by the buoys during the entire two-year period is denoted by the vertical line on January 4 in Fig. 5b.

During January, there was noticeable intraseasonal variation (\sim 10 30 day time scale) in the magnitudes of the cyclone-scale (3 7 days) high Q_{net} episodes. We show below that these are due to intraseasonal variations in the latitudinal position of the atmospheric jet stream (JS) along the longitude of PEACH (75°W), which tend to affect the tracks and the timing of intensification of the ETCs passing through PEACH. A similar period of intraseasonal change in the JS s position occurred in March 2018, which will also be described below.

4. Atmospheric forcing north and south of Cape Hatteras

The different SST levels on the continental shelf north and south of Cape Hatteras (more specifically, north and south of the Hatteras Front; see Figs. 1 and 4a,b) contribute to different levels of atmospheric forcing between the two regions (Fig. 4c,d). This is apparent in the stress and Q_{net} time series from Buoys B1 (north of Cape Hatteras) and B2 (south of Cape Hatteras), which are shown in Fig. 7. The clear coherence between the pairs of time series is due to the.

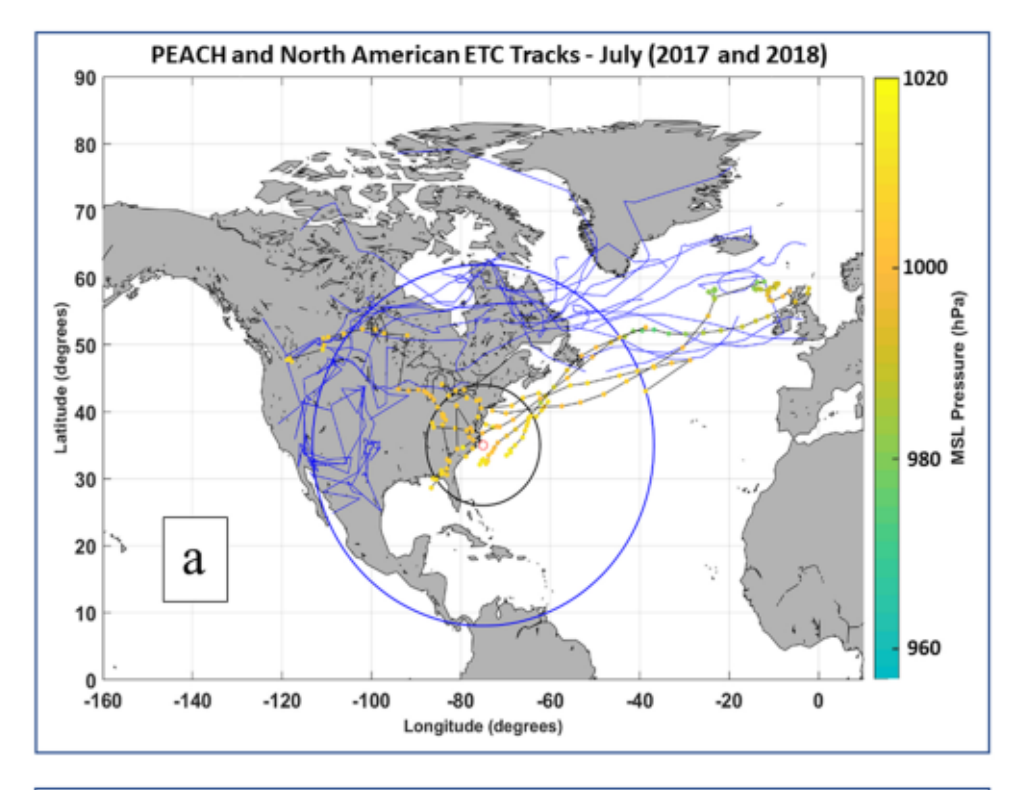
large lateral scale of the atmospheric systems causing the forcing, mostly ETCs (\sim 1000 km or more), in comparison to the separation distance between these 2 buoys (\sim 120 km). An important north-south difference is that B1 wind stress and Q_{net} magnitudes are nearly always less than those farther south, at B2, largely due to the cooler waters to the north of the Hatteras Front.

5. Extratropical cyclone tracks

ETCs are low-pressure-center, cyclonic (counter-clockwise in the northern hemisphere) circulations within the troposphere that are largely created by and evolve with eastward propagating mesoscale JS waves (Davis and Dolan, 1993; Palmen and Newton, 1969; Schultz and co-authors., 2019). To determine the tracks of ETCs during 2017 18, cyclonic wind systems were detected as local minima in the mean sea level atmospheric pressure field and followed through a series of maps constructed from the ERA5 dataset (Hersbach et al., 2018) from 1979 to 2019. We utilized a cyclone detection and tracking algorithm, adapted from mesoscale oceanic and atmospheric eddy tracking algorithms (Serreze, 1995; Chelton et al., 2011; Oliver et al., 2015), to determine cyclone tracks (based on positions every 6 h) for the region spanning North America and the Atlantic Ocean. As anticipated, relatively weak ETCs transited the Hatteras coastal ocean throughout the warm season, while ETCs transiting during the cool season were strong and frequent (nearly every several days).

5.1. Warm season ETC tracks

Tracks for those ETCs that progressed over eastern North America and the adjacent Atlantic Ocean such that their low-pressure



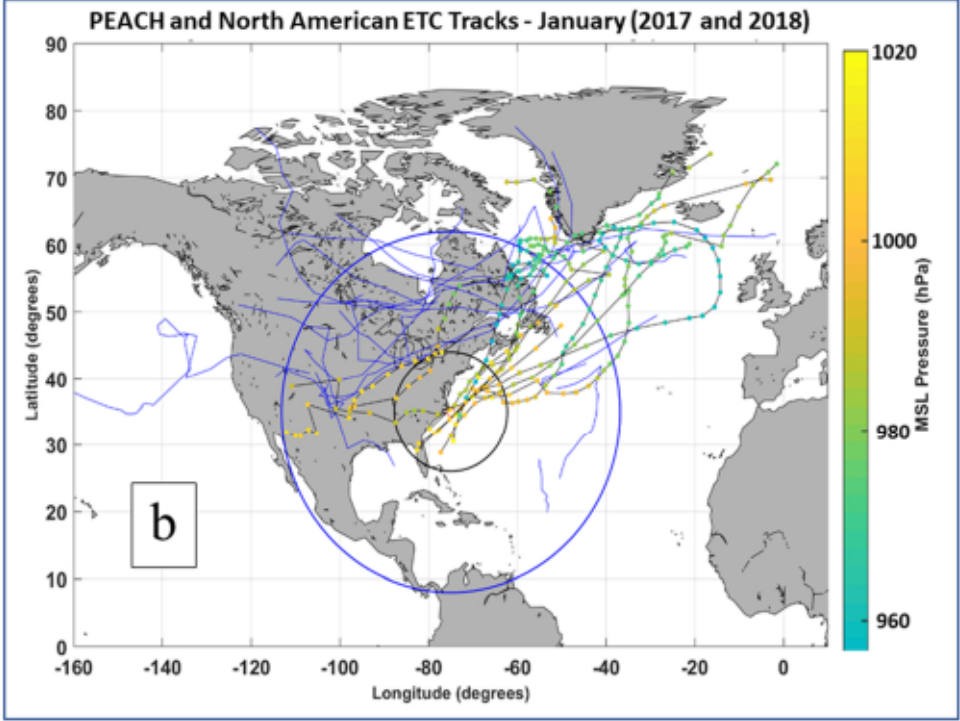


Fig. 8. Tracks for ETCs that originated in (a) July 2017 or July 2018 and (b) January 2017 or January 2018. Tracks with dots (cyclone centers every 6 h) are "PEACH cyclones" which passed within 1000 km of 35°N, 75°W. All tracks that passed within 3000 km of PEACH are "North American cyclones" (which includes PEACH cyclones). The PEACH cyclone tracks have colored dots, which denote the low-pressure-center position and pressure at 6-hour intervals. PEACH cyclone progression is southwest-to-northeast in essentially every case. The black (blue) circle is 1000 km (3000 km) in diameter and centered on 35°N, 75°W.

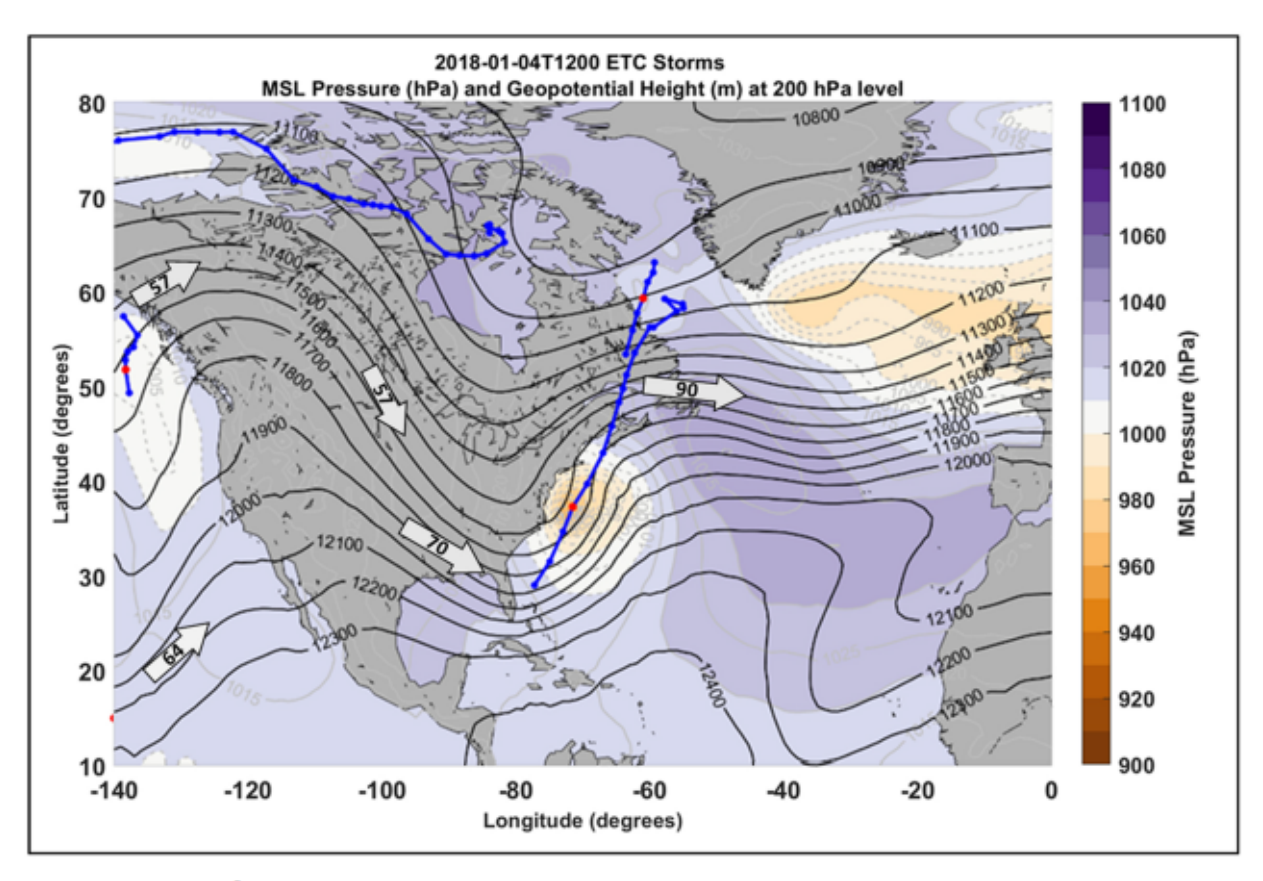


Fig. 9. Weather map for January 4, 2018 at 1200 UTC. The background shading and accompanying contour lines show the surface atmospheric pressure field. ETC Grayson was located just northeast of Cape Hatteras and can be seen in the circular tan shading. Blue and red dots show the tracks of surface low-pressure centers (cyclones), with dots at 6-hour intervals. Red dots show cyclone locations at the time of this map. The solid black lines show geopotential height (m) of the 200 hPa atmospheric pressure surface. Two JSs on that pressure surface (arrows with wind speeds, m s⁻¹) were flowing into the panel from the west following the closely spaced height contours, and they merged into one over central North America. A JS trough was located roughly along 80°W. ETC Grayson was located between this trough and the JS crest located roughly along 60°W. This is a typical relative positioning of amplifying ETCs and JS waves (Wallace and Hobbs, 2006).

centers passed within 3000 km of the central PEACH region (35°N, 75°W) during July 2017 and July 2018 are shown in the composite in Fig. 8a. All of these tracks went through the blue circle (3000 km radius), and they are referred to herein as "North American cyclones". The subset of these ETCs that passed within 1000 km of the central PEACH region passed through the black circle (1000 km radius), and we call these "PEACH cyclones". They are representative of the cyclones affecting the Hatteras coastal ocean. The PEACH cyclone tracks have colored dots, which denote the low-pressure-center position and pressure at 6-hour intervals. PEACH cyclone progression is southwest-to-northeast in essentially every case. These July tracks are representative of the ETC tracks during the 2017 and 2018 warm seasons.

5.2. Cool season ETC tracks

Fig. 8b shows a composite of North American cyclone tracks from January 2017 and January 2018 (PEACH cyclone tracks again have colored dots). The typical SW-to-NE progression of the PEACH cyclones is apparent in each panel, and this is typical of almost all ETCs passing through the PEACH circle year-round. The non-PEACH North American cyclones typically moved west-to-east across North American orth of the PEACH circle. In monthly counts, PEACH cyclones typically accounted for around 20–30% of North American cyclones, as defined herein (expanded upon in Section 7 below).

One example of a cool season ETC is shown in Fig. 9, which is a snapshot of the surface and 200 hPa pressure fields on January 4, 2018. The cyclone that is apparent just northeast of Cape Hatteras was, as described above, the strongest ETC affecting PEACH during all of 2017–18, and it developed (i.e., its central low pressure decreased) rapidly enough that it was classified a "bomb" cyclone (Hirata et al., 2019). The lateral extent (diameter) of this cyclone was ~1500 km. Most ETCs that passed over the Hatteras coastal ocean during PEACH were around 1000–2000 km in lateral extent, as determined from surface pressure fields.

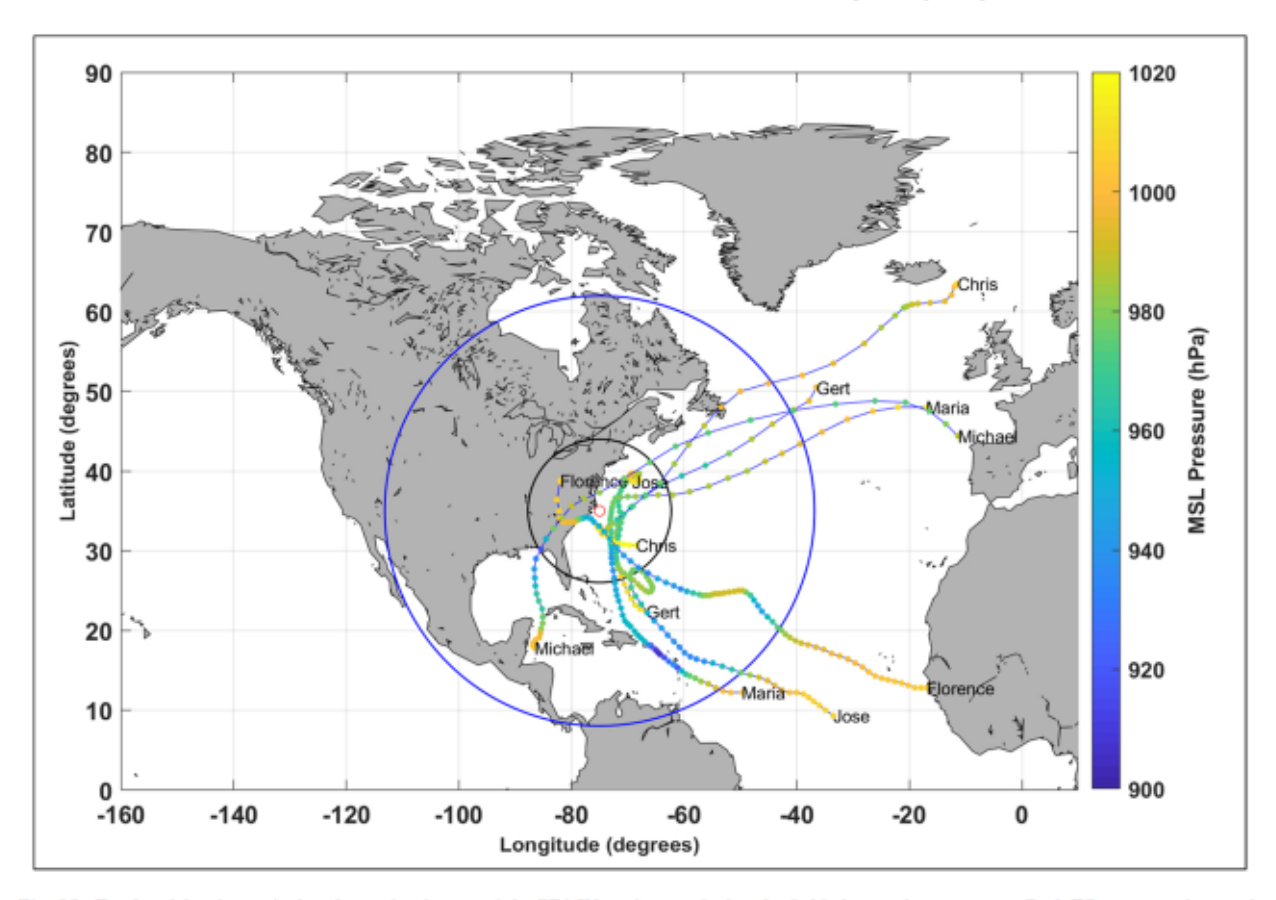


Fig. 10. Tracks of the six tropical cyclones that impacted the PEACH study area during the field observations program. Each TC progressed towards higher latitude for most or all of its lifetime. The two circles here are the same as in Fig. 8.

6. Tropical cyclones

Tropical cyclones (TCs; tropical storms with sustained wind speeds 13–33 m s⁻¹, and hurricanes with sustained wind speeds >33 m s⁻¹) occur in the North Atlantic mostly during the "Hurricane Season" (June 1 through November 30: NOAA., 2022b). Six hurricanes impacted the PEACH region during the 2017–18 field observations program (Fig. 10): Gert, (Aug 14–17, 2017), Jose (Sept 18–19, 2017), Maria (Sept 25–28, 2017), Chris (July 7–10, 2018), Florence (Sept 12–15, 2018), and Michael (Oct 10–13, 2018), where the dates indicate the time periods in which wind stress at PEACH was clearly from a TC. Wind stress pulses from two of these TCs are indicated above in Fig. 5a. In comparison to the relatively common SW-to-NE ETC tracks,

the TC movements are quite varied in direction and speed as they crossed over or near PEACH, and so the magnitude and direction of wind stress there varied greatly from one TC to another. For example, Hurricane Chris transited northeastward during early July along a track that was about 200–300 km offshore of PEACH. The generally southeastward wind stress from this hurricane was recorded in all 5 buoys, two of which are shown in Fig. 5a. Hurricane Florence approached the southern coast of North Carolina along a northwestward-then-westward track that passed just south of PEACH (Zambon et al., 2021), and the wind stress at PEACH was quite strong and generally westward (Fig. 5a).

7. Long-term variations in NAO and in ETC numbers and strength

It is of interest to know how typical the atmospheric processes were during PEACH. In particular, have the number and/or strength of ETCs passing over the Hatteras coastal ocean changed in recent years and decades? The top panel in Fig. 11 shows a 41-year-long time series (1979 through 2019) of the number of cyclones that have passed through the North American circle, and the subset through the PEACH circle. The center panel shows the collective "strength" of the North American cyclones in each season. Strength here is taken to be the season-average minimum-central-pressure of the ensemble of North American cyclones in each season. (Bach individual cyclone's minimum central pressure can have occurred anywhere along

the cyclone's entire track, even if it occurred outside of the North American circle.) The bottom panel shows the season-averaged NAO Index for the same 41-year time period. The least-squares linear fit line to each of the time series in the top two panels has a slope that is not significantly different from zero. Multi-year variations are apparent in each of these time series, with amplitudes of +/-

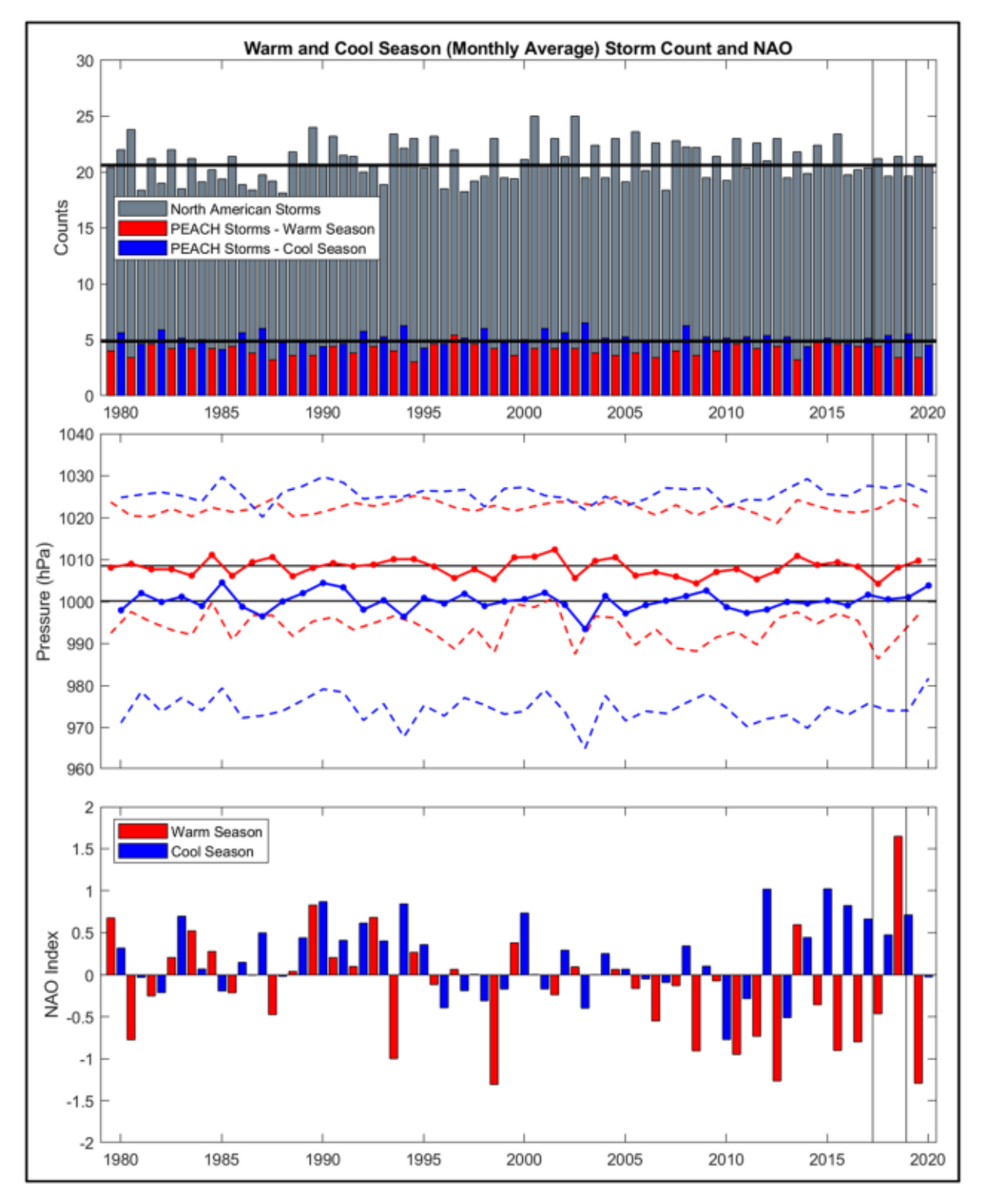


Fig. 11. Monthly-averaged number of ETCs that passed through the PEACH circle and through the North American circle in each warm season and each cool season (top); the season-average minimum-central-pressure (solid lines) and +/-1 standard deviation (dashed lines) of all cyclones progressing through the North American circle during each season (middle); and the NAO Index for each season (bottom). Each panel is for 1979 through 2019. The North American counts include PEACH counts for each season. The least-squares best-fit line through the variable in the top two panels are shown, each of which is not significantly different from zero. The PEACH time period is denoted by the two vertical lines on the right.

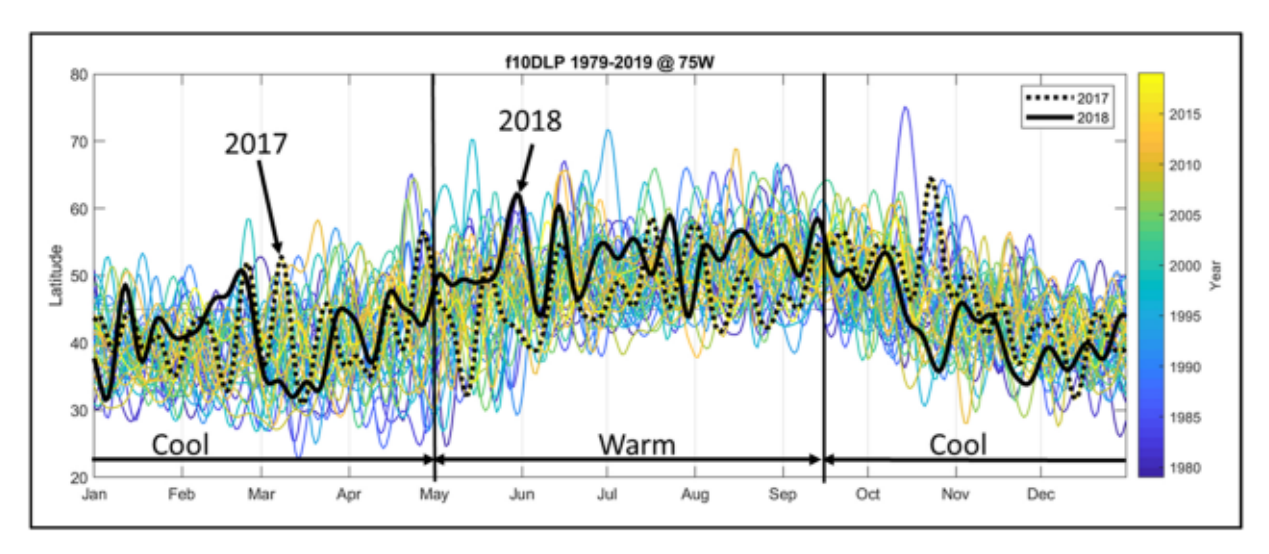


Fig. 12. The latitude of the JS along 75°W longitude, for each year from 1979 through 2019. The latitude position was determined every six hours from ERA5 data, and those time series were 10-day low-pass filtered. When more than one JS core was apparent, the stronger core was selected. The 2017 and 2018 time series are highlighted in black.

several monthly-averaged counts around the zero-slope linear-fit line. Comparing the number and strength time series with the NAO Index bar graph does not reveal a clear correlation.

8. Atmospheric jet stream effects

Typically, one or more JSs are flowing over North America and the western North Atlantic at any given time. A JS is a strong, generally-eastward-flowing wind jet that is O(1000 km) wide, and it's velocity-maximum (speed ~50-100 m s⁻¹) is often centered within the tropopause, around the 200 hPa level (Reiter, 1963; Rikus, 2015). The importance of JSs here is that the tropospheric ETCs that drive much of the variability in air-sea heat and momentum fluxes in the Hatteras coastal ocean are an inherent part of a JS's lateral (north-south) shortwave motions, which propagate eastward with a typical periodicity ranging from 2 to 10 days (Attard and Lang, 2017; Palmén and Newton, 1969; Sanders, 1988). On occasion, one JS can bifurcate into two, or two JSs can merge into one. In Fig. 9, for example, two JSs can be seen entering the panel through its western edge, one from about 10–20°N latitude, and the other from about 50–70°N. These two jets merge into one over central North America.

ERA5 4D data (Hersbach et al., 2018) were used to determine JS locations (latitude, longitude and pressure level) every 6 h. From this dataset, the variable path of the strongest winds in the upper atmosphere (12 levels, between 500 and 100 hPa) was extracted for a 41 year period (1979–2019). The JS location at each longitudinal slice was identified by finding the latitude and pressure level of the local maxima windspeeds (greater than 40 m s⁻¹) following Rikus (2015) and Manney, et al. (2011). When more than one JS core was apparent, the stronger core was selected. The Jet Stream Visualization Tool (jsviz, Haines, 2021) provides maps and vertical sections of high-wind features, from which JS locations were found and cataloged in the long-term time series.

The latitude of the selected JS along longitude 75°W was determined every 6 h for each year from 1979 through 2019. The 41 JS latitude position time series thus determined were then 10-day low-pass filtered, and these are displayed in Fig. 12. The purpose of the 10-day filtering is to show the slowly varying (intraseasonal and longer period) latitude of the JS, around which the ETC-associated JS shortwaves fluctuated.

Note that the JS was south of its typical location during early January 2018, when ETC Grayson was generated off southeastern Florida. As Grayson tracked along the path of the Gulf Stream towards Cape Hatteras, it extracted a large amount of heat from the Stream, and this thermal forcing of the lower atmosphere together with the JS wave forcing contributed significantly to the explosive development of this particular ETC, which ultimately brought the strongest episode of wind stress to PEACH. We refer the reader to the more in-depth analysis of Grayson presented in Hirata et al. (2019). Most of March 2018 was another period of a southern intraseasonal JS location. During this time, several strong ETCs progressed through PEACH. High wind stress and Q_{net} values occurred then (see Figs. 5b, 12). Similar JS intraseasonal oscillations have been implicated in bringing ETCs tracks into and out of a coastal area along the northwestern U.S. (Bane et al., 2005, 2007).

9. Oceanic responses to atmospheric forcing

9.1. Oceanic response to wind stress

The early study by Savidge and Bane (2001) and the PEACH analysis by Han et al. (2022) have shown that along-shelf oceanic volume transport variability is primarily wind-driven, while along-shelf volume transport convergence (and thus shelf-ocean

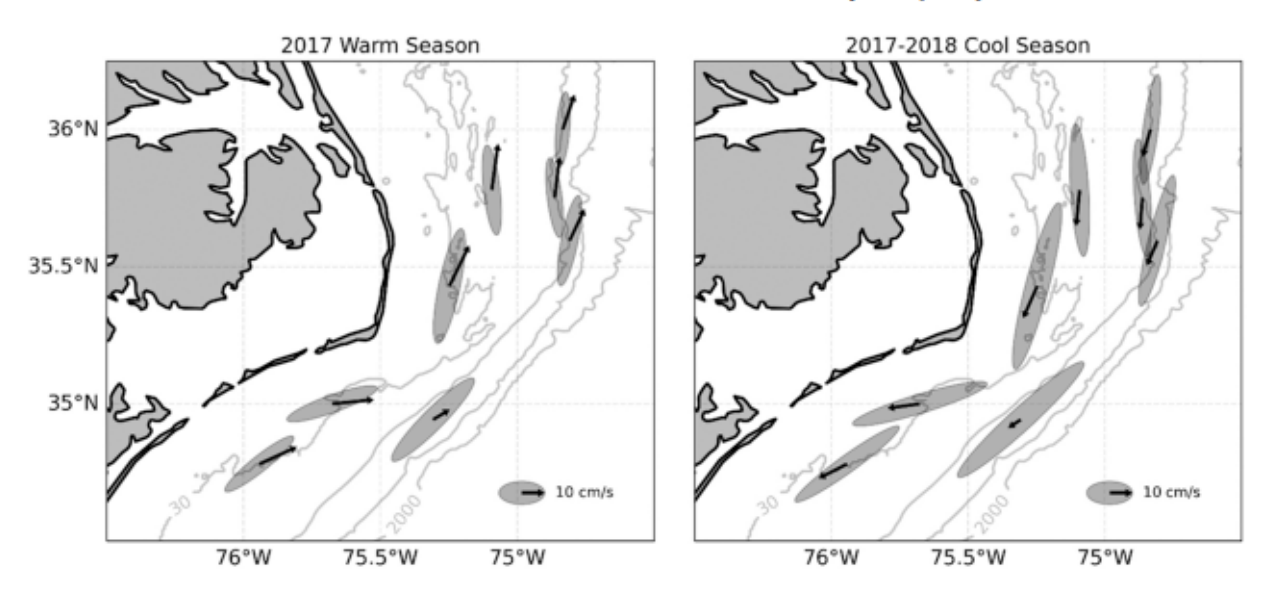


Fig. 13. The upper-layer (top 1/3 of the water column) mean ocean currents at 8 PEACH moorings (arrows), and the standard deviation ellipses of the first eof mode of the current variations about the means. The left (right) panel is for the 2017 warm season (2017–2018 cool season).

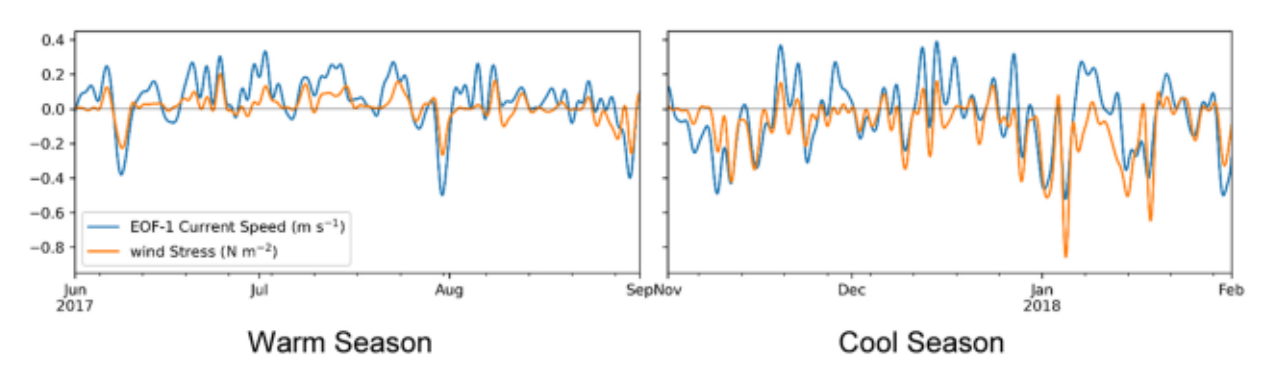


Fig. 14. Three-month-long time series of wind stress (orange) and eof-1 currents (blue) extracted from the 2017 Warm Season (left) and 2017–18 Cool Season (right). These time series are from Buoy B-1, and have been 40-hour-low-pass filtered. The wind stress has been lagged by 9 h in each panel, to account for the wind-driven current spin-up time. Visually, the coherence between the wind stress and current variations is apparent. The 18-month-long Pearson correlation coefficient for these two variables is 0.68.

Table A1
Sensors, variables measured, sampling height/depth, and sampling rate.

Instrument	Measurements	Height/depth	Sampling rate
RM Young anemometers model 5106	Wind speed and direction	3.0 m, 3.25 m	6 min
Vaisala HMP-45 C	Air temperature and relative humidity	1.5 m	6 min
Eppley PSP	Downward shortwave radiation	2.75 m	6 min
Eppley PIR	Downward longwave radiation	2.75 m	6 min
RM Young aiphoning bucket model 5020	Rain rate	2.75 m	6 min
Vaisala PTB100	Barometric pressure	1.5 m	6 min
Seabird microcata 37 IMP, 37 SMP	Seawater conductivity, temperature and pressure	-2 m, - 15 m, - 30 m	6 min
TRDI 600 kHz Workhorse ADCP	Current profiles and directional surface waves	Pull water column	Currenta 30 min,
			Waves 12 h

exchange) is highly correlated with Gulf Stream position offshore. Following the work by Han et al. (2022), we have used empirical orthogonal function (eof) analyses of PEACH wind stress and ocean current data to show that 41% of the ocean current variability in the Hatteras coastal ocean is contained eof mode-1, and this mode is highly correlated with local wind stress variations (correlation coefficient is 0.68). Fig. 13 shows the seasonal-mean upper-layer (1/3 of the water column) currents are closely aligned with isobaths and generally oriented towards Cape Hatteras: north of Cape Hatteras over the MAB, the mean currents are southward (cool season) or weak (warm season); southwest of Cape Hatteras over the SAB, the mean currents are northeastward (both seasons). Also shown are

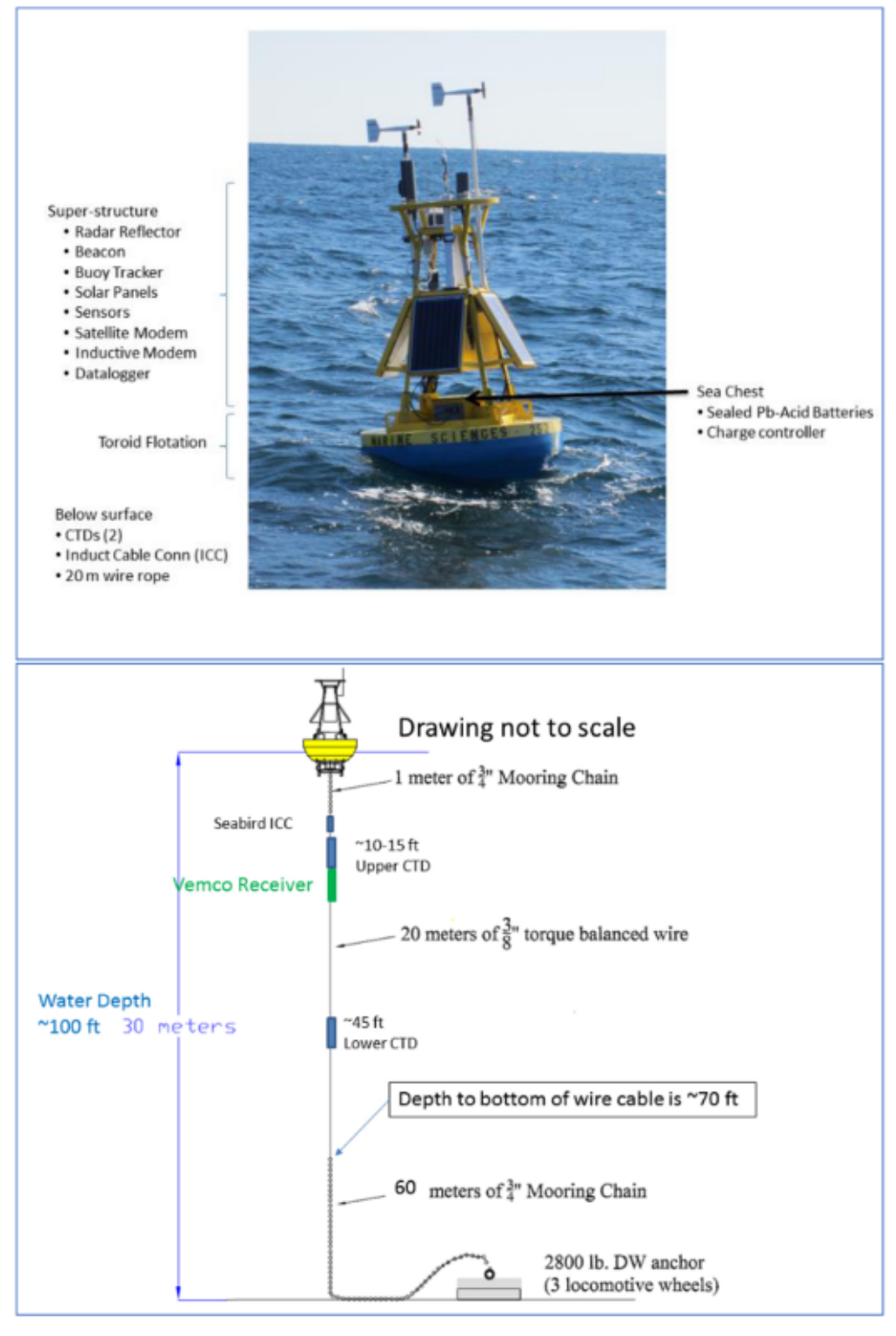


Fig. A1. Photo of buoy (top) and schematic of buoy mooring design (bottom).

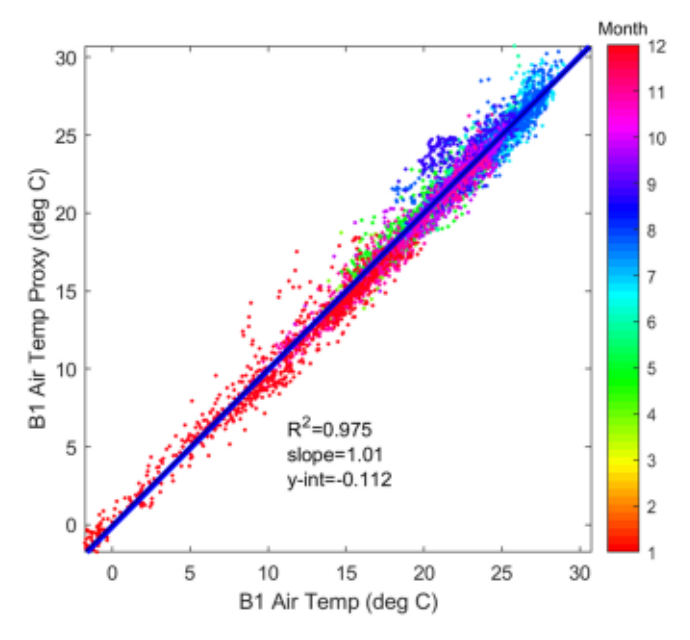


Fig. A2. Scatter plot of B1 Air Temp vs Air Temp Proxy. One-to-one line (thin line) and linear regression (thick line) with fit metrics are shown.

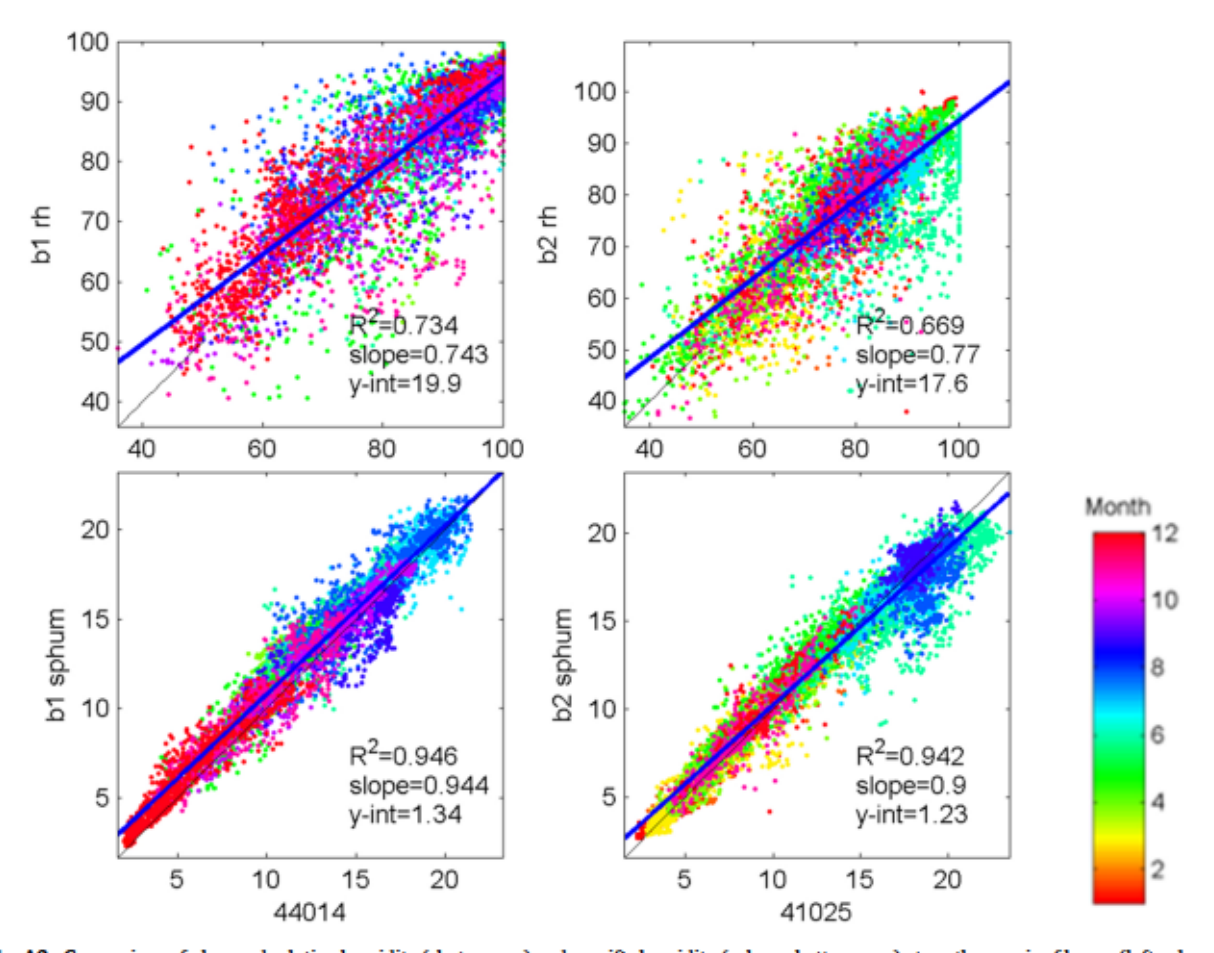


Fig. A3. Comparison of observed relative humidity (rh, top row) and specific humidity (sphum, bottom row) at northern pair of buoys (left column) and southern pair of buoys (right column). One-to-one line (line black) and linear regression (thick line) with fit metrics are included for each comparison.

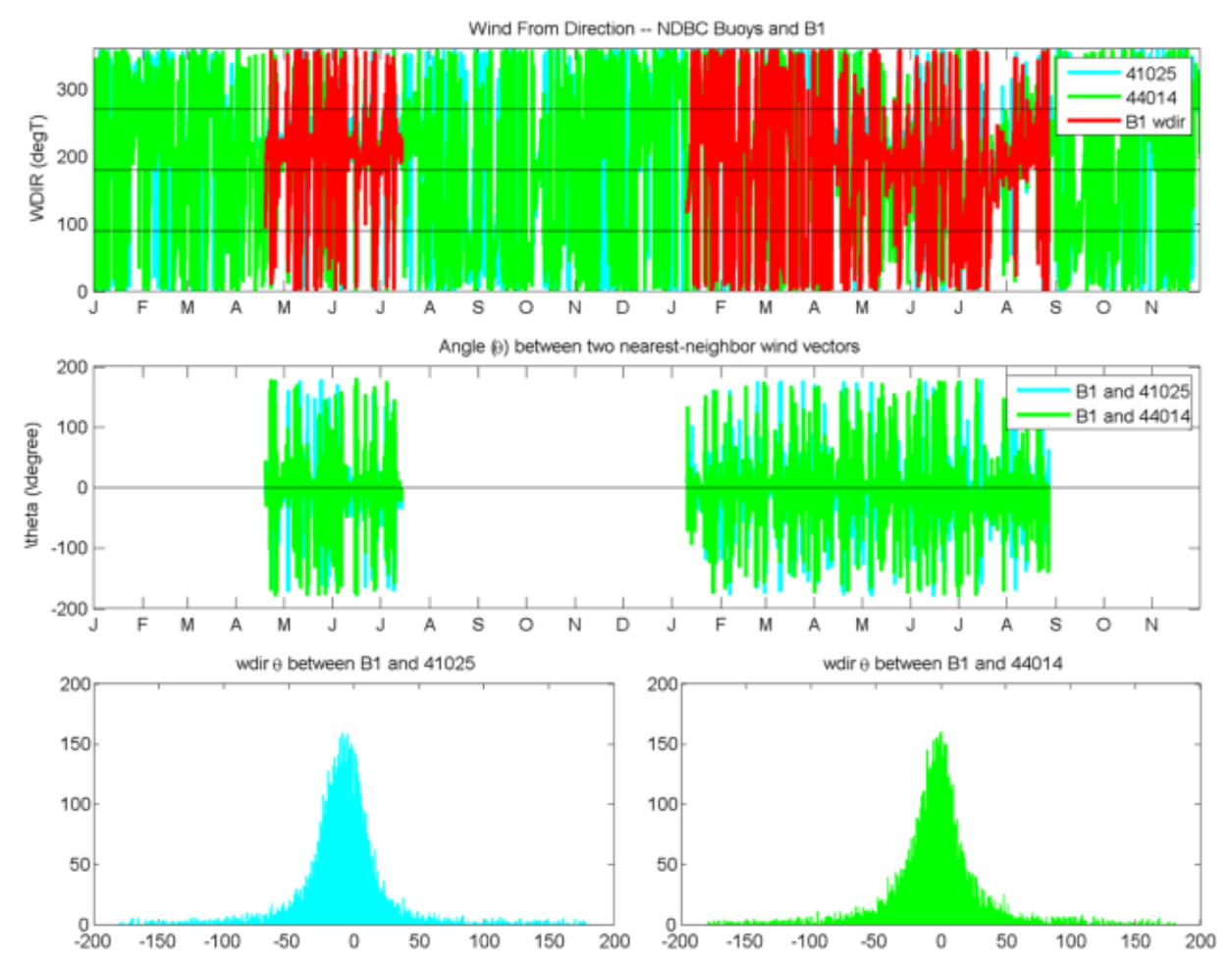


Fig. A4. (top) observed wind direction at NDBC buoys 41025 and 44014 and UNC buoy B1, showing time period when B1 direction was functioning; (middle) difference in wind direction between B1 and the NDBC buoys; (bottom) distribution of wind direction differences in middle panel, indicating 44014 and B1 shown near-zero bias.

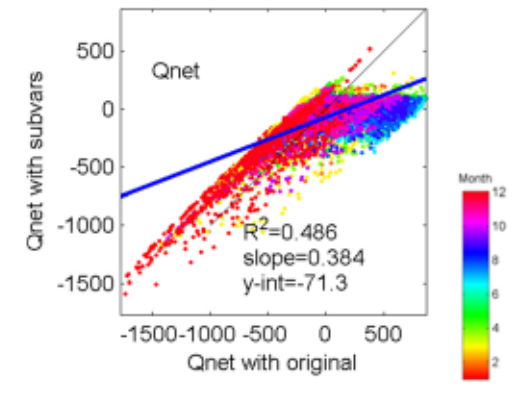


Fig. A5. Comparison of net heat flux (Qnet) at buoy B2 formed using observed short- and long-wave downwelled radiation (original) and with default values in COARE 3.6 algorithm (subvars). Because of the poor comparison, short- and long-wave downwelled radiation values were substituted at NDBC buoys instead of using default values.

the eof-1 standard deviation ellipses for these currents during each season. The coherence between the wind stress and the currents is evident in Fig. 14, which shows the wind stress from Buoy B-1 along with the current variations in eof-1 at that location.

9.2. Oceanic response to surface heat flux

During the warm season, net heat flux across the air-sea interface is dominated by solar radiation into the into the ocean. The main oceanic response over the continental shelf is an increase in water temperature, and thus the near-surface air temperature and near-surface water temperature remain within about a degree Centigrade of each other (Fig. 7). Cool season ocean-to-atmosphere net heat fluxes become large and out of the ocean during the passage of ETCs, particularly following the passage of the ETC s cold front. These episodes of oceanic heat loss decrease the shelf water temperatures (Atkinson et al., 1989) and temperatures in the adjacent Gulf Stream (Bane and Osgood, 1989).

A new PEACH finding is reported in Han et al. (2021), who observed a shelf water cascading event that has both wind stress and ocean-to-atmosphere heat flux as drivers. Episodes of strong cooling (high Q_{net} caused by cold air flow during the cool season) can generate downward convection of shelf surface waters, which then can cascade downslope across the shelf as a gravity current to meet the Gulf Stream along the upper continental slope. The cascading waters then enter the Stream along their matching isopycnal surfaces, thereby exiting the shelf. Following first-hand observation of this process made during a PEACH cruise in January 2018, five other cascading events were found in historical data between 2014 and 2016, demonstrating that this is a typical cool season process in the Hatteras coastal ocean.

10. Summary and outlook

The atmosphere forces the Hatteras coastal ocean in two important ways: (i) through surface wind stress (approximately 40% of the shelf current variance can be attributed to wind stress fluctuations) and (ii) through ocean-to-atmosphere heat fluxes. Observations made during 2017 18, encompassing the PEACH field program, have shown that these processes can be described in terms of two seasons: the warm season (May through mid-September), with predominantly mild northeastward winds punctuated by an occasional TC passing through the region; and the cool season (mid-September through April), with a nearly continuous, northeastward progression of energetic ETCs through the region. Cool season ETCs force the ocean with strong wind stress and ocean-to-atmosphere heat flux episodes, each with a time-scale of a few days. TC passages are much less frequent than ETCs, as anticipated, and have widely varying tracks in comparison to the typical SW-NE movements of ETCs. Outside of TCs, wind stress fluctuation magnitudes typically exceed mean stress magnitudes by a factor of 3 5. Q_{net} is typically into the ocean throughout the warm season at around 50 100 W m⁻², while it is essentially always out of the ocean during the cool season, with large ocean heat loss episodes of 500 1000 W m⁻² or more due to cold airflow over the region associated with passing ETCs.

During the 41 years leading up to and through PEACH, North American cyclone numbers and strength showed multi-year variations but no long-term trends. Additionally, no apparent correlation with NAO was found. Although we did not report separately here on strength variations in TCs that moved through the region, Paerl et al. (2019) found for coastal North Carolina, . a period of unprecedentedly high precipitation since the late-1990 s, and a trend toward increasingly high precipitation associated with tropical cyclones over the last 120 years.

An important aspect of our description of the region s atmospheric processes during PEACH is that activities are presently ramping up here. The NSF Pioneer Array is scheduled to be relocated here in 2024, and this promises to provide continuous, multi-year atmospheric and oceanic observations in the northern portion of the Hatteras coastal ocean (Pioneer Array Relocation., 2023). Additionally, the NASA SWOT satellite has begun its ocean topography mission, which has a ground-track cross-over within the region (Morrow et al., 2019).

CRediT authorship contribution statement

John Bane: Conceptualization; Formal analysis; Funding acquisition; Investigation; Methodology; Supervision; Roles/Writing - original draft; Writing - review & editing, Harvey Seim: Funding acquisition; Investigation; Methodology; Project administration; Supervision; Writing - review & editing, Sara Haines: Data curation; Formal analysis; Methodology; Software; Validation; Visualization; Writing - review & editing, Lu Han: Data curation; Formal analysis; Methodology; Software; Visualization; Writing - review & editing, Ruoying He: Conceptualization; Funding acquisition; Investigation, Joseph Zambon: Conceptualization; Investigation.

Declaration of competing interest

The authors declare that they have no known competing financial interests or personal relationships that could have appeared to influence the work reported in this paper.

Data availability

Data will be made available on request.

Acknowledgments

We gratefully acknowledge support for the PEACH program from the National Science Foundation (OCE-1558920 to UNC-CH, OCE-1559178 to NCSU, OCE-1559476 to Skidaway Inst., OCE-1558521 to Woods Hole Ocean. Inst.). The ship and technical crews aboard the *R/V Armstrong* during 3 PEACH cruises are heartily thanked for their always capable direction and assistance. The authors declare no conflicts of interest.

Software availability statement

Version 1.0 of the Jet Stream Visualization Tool (jsviz, Haines, 2021) used for cataloging the long-term time series of jet stream locations is preserved at https://doi.org/10.5281/zenodo.4570931 and developed openly at https://github.com/neaptide/jsviz.

The storm tracking computer code (Chelton et al., 2011, Oliver et al., 2015) used for cyclone detection and tracking is available publicly online at https://github.com/ecjoliver/stormTracking.

Version 3.6 of the Coupled Ocean-Atmosphere Response Experiment (COARE) bulk flux algorithm (Edson et al., 2013) used to estimate heat flux and wind stress at each buoy is available publicly at ftp://ftp1.esrl.noaa.gov/BLO/Air-Sea/bulkalg/cor3 6/.

Appendix

Collection and processing of heat and momentum fluxes during PEACH

This appendix describes the collection and processing of meteorological observations during the PEACH program used to produce estimates of momentum and heat flux between the ocean and atmosphere. The meteorological buoys used, instrumentation supported, quality control steps taken, and data recovery are reviewed, along with actions taken to substitute or develop proxies where necessary to have sufficient input for the flux calculations. The sensitivities of the bulk formulae flux calculations to some inputs are examined.

The two buoys deployed by UNC, designated B1 and B2, were purchased from the University of Maine, where they were designed and built (Wallinga et al., 2003). The buoys consist of a 2 m toroid with a well that holds batteries and a charge controller and a 2.75 m tall superstructure that holds four solar panels. Each buoy was deployed on a single-point mooring in 30 35 m water depth, consisting of 20 m of jacketed wire rope, a swivel and 60 m of chain to a 2800 lbs anchor (stack of 3 locomotive wheels). The superstructure was instrumented with the meteorological sensors listed in Table A1. Duplicate anemometers were mounted on Delron rods that could be raised and lowered to avoid damage during deployments and recoveries. Short- and long-wave downward radiation sensors (PSP an PIR) were mounted on the top surface plate of the superstructure, with air temperature/relative humidity and rain gauge sensors and a barometer port mounted lower on the superstructure, along with cannisters holding the data acquisition system components (Fig. A1). A near-surface and mid-depth CTD were deployed on the jacketed wire rope with communications supported by an inductive modem. A separate.

bottom frame was deployed outside the watch circle of the buoy and held an upward-looking ADCP, which sampled both currents and surface waves, and included a near-bottom CTD.

The data acquisition system sampled the instruments in Table A1 at the sample rate listed in the table, resulting in a regular time series every 6 min. These data were recorded internally, and transmitted hourly via Iridium to shore. The 6-minute observations were quality controlled (QC) using a mix of automated tests (sensor health, range/threshold, and time-continuity) and manual elimination (known events, graphical analysis), then averaged to hourly values. Sensor-specific QC steps included wind direction comparisons with nearby NDBC buoys (40125 and 44014). Each buoy suffered some damage from strong storms (Hurricane Jose, ETC Grayson and Hurricane Florence each caused some sensor failures on one of the buoys), resulting in data gaps and replacement of some sensors over the PEACH field program. Each buoy was recovered, serviced and redeployed during the PEACH turnaround cruise (AR-26) approximately 9 months after their initial deployment.

Heat and momentum fluxes (stresses) were calculated with observations from B1 and B2 (the UNC buoys) and with observations from NDBC buoys 44014, 41025 and 41064 using the COARE 3.6 algorithms (Edson et al., 2013). These algorithms require inputs of wind speed and direction, air and water temperature, relative humidity, downward short- and long-wave radiation, air pressure and rain rate and include optional inputs of surface salinity, ocean current speed and direction, and surface wave height and speed. All of these variables are available from the UNC moorings. The NDBC moorings lack downward short- and long-wave radiation, rain rate, salinity and ocean current speed and direction.

For the UNC buoys, because of data gaps resulting from sensor damage in storms, possible substitutions for variables used in the COARE 3.6 algorithms were explored. The temperature/relative humidity sensor required the greatest percentage of substitutions. For air temperature, it was found that the internal temperature sensor in the data acquisition cannister was a valid proxy for measured air temperature using an unweighted smoothing spline fit based on the difference between the canister and outside temperature sensors and the hour of the day when both sensors were functioning. The observed and proxy air temperatures are compared in Fig. A2. This air temperature substitution accounted for 55% of the observations at B1 and 0% at.

B2 (the latter record ends in September 2018 because both the canister temperature sensor and temperature/humidity sensor failed during Hurricane Florence). For relative humidity, we sought to use measurements from a nearby buoy to fill data gaps. However, significant variations in air temperature between buoy locations led to strong variations in relative humidity. However, specific humidity (the ratio of the mass of water vapor to mass of air) was found to be consistent between some pairs of buoys (Fig. A3). We used times when all buoys were operative.

to identify buoys that typically observed similar specific humidity. For times when relative humidity was missing from a buoy record, we substituted specific humidity from an adjacent buoy, then corrected to relative humidity using the local air temperature measurement. This substitution was used 55% of the time at B1 and 20% of the time at B2. The other primary substitution was for wind direction at B1; the speed sensor functioned correctly for the entire deployment but direction was not reported for 45% of the record. Comparisons were made using times when wind direction was available from B1 with NDBC buoys 44014 (to the northeast) and 41025 (to the south). It was found that wind direction at 44014 was most similar to those at B1, with essentially no bias and a small spread of differences (Fig. A4). Use of these.

substitutions for relative humidity and wind direction at B1 results in net heat flux values very similar to those observed (fit with slope 1.01 and $R^2 = 0.992$).

For the NDBC buoys, sampling was averaged to hourly values as needed. Downward short- and long-wave radiation were not measured by these platforms. There are default values for these in the COARE 2.0 (which include a latitudinal dependence and cloud fraction estimate) and COARE 3.6 (which use constant values) algorithms; the impact of using these versus the measured values were assessed using the observations from the UNC buoys (B1 and B2). It was found that the net heat flux formed using default values versus measured values of the downward short- and long-wave radiation were poorly correlated (Fig. A5). We therefore substituted time histories of downward short- and long-wave radiations from either B1 or B2 for the 3ND BCE buoys depending on proximity.

A series of sensitivity tests were conducted to assess the importance of and desirability of including optional inputs. Surface current was not available at the NDBC buoys. Net heat fluxes formed at B1 and B2 with and without inclusion of surface currents were nearly identical, a consequence of relatively low current speeds. Because none of the NDBC buoys are deployed in the Gulf Stream, it is expected that the impact of not correcting the wind speed for surface current on the fluxes will also be minimal. Sensitivity of the fluxes to inclusion of surface salinity and rain rate were also explored at B1 and B2, and again found to result in minimal differences. It was therefore decided to form the fluxes at the NDBC buoys without inclusion of surface current, salinity or rain rate.

The full dataset is available at Haines et al. (2022).

References

Andres, M., 2021. Spatial and Temporal Variability of the Gulf Stream Near Cape Hatteras. J. Geophys. Res. 126. https://doi.org/10.1029/2021JC017579.

Atkinson, L., Lee, T., Blanton, J., Chandler, W., 1983. Climatology of the southeastern United States continental shelf waters. J. Geophys. Res. 88, 4705 4718. https://doi.org/10.1029/JC088iC08p04705.

Atkinson, L., Oka, E., Wu, S., Berger, T., Blanton, J., Lee, T., 1989. Hydrographic variability of southeastern United States shelf and slope waters during the Genesis of Atlantic Lows Experiment: Winter 1986. J. Geophys. Res. 94, 10699 10713. https://doi.org/10.1029/JC094iC08p10699.

Attard, H., Lang, A., 2017. Climatological and case analyses of lower-stratospheric fronts over North America. Q. J. R. Meteorol. Soc. 143, 1471 1484. https://doi.org/10.1002/qj.3018.

Austin, J., Lentz, S., 1999. The relationship between synoptic weather systems and meteorological forcing on the North Carolina inner shelf. J. Geophys. Res. 104, 18159 18185. https://doi.org/10.1029/1999JC900016.

Bane, J., Levine, M., Samelson, R., Haines, S., Meaux, M., Perlin, N., Kosro, P., Boyd, T., 2005. Atmospheric forcing of the Oregon coastal ocean during the 2001 upwelling season. J. Geophys. Res. 110. https://doi.org/10.1029/2004JC002653.

Bane, J., Osgood, K., 1989. Wintertime air-sea interaction processes across the Gulf Stream. Journal of Geophysical Research 94, 10755 10772. https://doi.org/10.1029/2004JC002653.

Bane, J., Spitz, Y., Letelier, R., Peterson, W., 2007. Jet stream intraseasonal oscillations drive dominant ecosystem variations in Oregon s summertime coastal upwelling system. Proc. Natl. Acad. Sci. 104, 13262 13267. https://doi.org/10.1073/pnas.0700926104.

Benedict, J., Lee, S., Feldstein, S., 2004. Synoptic view of the North Atlantic Oscillation. J. Atmos. Sci. 61, 121 144. https://doi.org/10.1175/1520-0469(2004)061% 3C0121:SVOTNA%3E2.0.CO.

Chelton, D., Schlax, M., Samelson, R., 2011. Global observations of nonlinear mesoscale eddies. Prog. Oceanogr. 91, 167–216. https://doi.org/10.1016/j.pocean.2011.01.002.

Csanady, G., Hamilton, P., 1988. Circulation of slopewater. Cont. Shelf Res. 8, 565 624. https://doi.org/10.1016/0278-4343(88)90068-4.

Davis, R., and Dolan, R. (1993). Nor easters. American Scientist, 81, 428 439. JSTOR, www.jstor.org/stable/29775010.

Davis, R., Hayden, B., Gay, D., Phillips, W., Jones, G., 1997. The North Atlantic Subtropical anticyclone. J. Clim. 10, 728 744 https://doi.org/10.1175/1520-0442 (1997)010<0728:TNASA>2.0.CO;2.

Edson, J., Jampana, V., Weller, R., Bigorre, S., Plueddemann, A., Fairall, C., Miller, S., Mahrt, L., Vickers, D., Hersbach, H., 2013. On the exchange of momentum over the open ocean. J. Phys. Oceanogr. 43, 1589 1610. https://doi.org/10.1175/JPO-D-12-0173.1.

Haines, S. (2021). jsviz: Jet Stream Visualization Tool (v1.0). Zenodo. https://doi.org/10.5281/zenodo.4570931.

Haines, S., Seim, H. and Bane, J. (2022). Processed Buoy and Heat Flux Data for the Processes Driving Exchange at Cape Hatteras (PEACH) Program (Level 2 – v1.0). [Data set]. Zenodo. https://doi.org/10.5281/zenodo.6383242.

Han, L., Seim, H., Bane, J., Todd, R., Muglia, M., 2021. A shelf water cascading event near Cape Hatteras. J. Phys. Oceanogr. 51, 2021 2033. https://doi.org/10.1175/JPO-D-20-0156.1

Han, L., Seim, H., Bane, J., Savidge, D., Andres, M., Gawarkiewicz, G., Muglia, M., 2022. Ocean circulation near Cape Hatteras: observations of mean and variability. e2022JC019274 J. Geophys. Res.: Oceans 127. https://doi.org/10.1029/2022JC019274.

Hersbach, H., Bell, B., Berrisford, P., Biavati, G., Horanyi, A., Munoz Sabater, J., Nicolas, J., Peubey, C., Radu, R., Rozum, I., Schepers, D., Simmons, A., Soci, C., Dee, D., and Thepaut, J.-N. (2018). ERA5 hourly data on single levels from 1979 to present. Copernicus Climate Change Service (C3S) Climate Data Store (CDS). (Accessed 20 December 2020), 10.24381/cds.adbb2d47.

Hirata, H., Kawamura, R., Nonaka, M., Tsuboki, K., 2019. Significant impact of heat supply from the Gulf Stream on a superbomb cyclone in January 2018. Geophys. Res. Lett. 46, 7718 7725. https://doi.org/10.1029/2019GL082995.

Hurrell, J.W., Kushnir, Y., Ottersen, G., Visbeck, M., 2003. An overview of the North Atlantic oscillation. Geophys. Monogr. -Am. Geophys. Union 134, 1 36. https://doi.org/10.1029/134GM01.

Lee, T.N., Ho, W.J., Kourafalou, V., Wang, J.D., 1984. Circulation on the continental shelf of the southeastern United States. Part I: subtidal response to wind and Gulf Stream forcing during winter. J. Phys. Oceanogr. 14, 1001 1012. https://doi.org/10.1175/1520-0485(1984)014%3C1001:COTCSO%3E2.0.CO;2.

Lee, T.N., Yoder, J.A., Atkinson, L.P., 1991. Gulf Stream frontal eddy influence on productivity of the southeast U.S. continental shelf. J. Geophys. Res. 96, 22191 22205. https://doi.org/10.1029/2004JC002653 https://doi.org/10.1175/2007JP03767.1.

- Li, J., Sun, C., Jin, F., 2013. NAO implicated as a predictor of Northern Hemisphere mean temperature multidecadal variability (https://doi:). Geophys. Res. Lett. 40, 5497 5502. https://doi.org/10.1002/2013GL057877.
- Li, W., Li, L., Ting, M., Liu, Y., 2012. Intensification of Northern Hemisphere subtropical highs in a warming climate. Nat. Geosci. 5, 830–834. https://doi.org/10.1038/ngeo1590.
- Li, X., Pichel, W., Maturi, E., Clemente-Colon, P., Sapper, J., 2001. Deriving the operational nonlinear multichannel sea surface temperature algorithm coefficients for NOAA-15 AVHRR/3. Int. J. Remote Sens. 22, 699 704. https://doi.org/10.1080/01431160010013793.
- Manney, G., Hegglin, M., Daffer, W., et al., 2011. Jet characterization in the upper troposphere/lower stratosphere (UTLS): Applications to climatology and transport studies. Atmos. Chem. Phys. 11, 1835 1889. https://doi.org/10.5194/acpd-11-1835-2011.
- Morrow, R., Fu, L., Ardhuin, F., Benkiran, M., Chapron, B., Cosme, E., d Ovidio, F., Farrar, J., Gille, S., Lapeyre, G., Le Traon, P.-Y., Pascual, A., Ponte, A., Qiu, B., Rascle, N., Ubelmann, C., Wang, J., Zaron, E., 2019. Global observations of fine-scale ocean surface topography with the surface water and ocean topography (SWOT) mission. Front. Mar. Sci. 6 232. https://doi.org/10.3389/fmars.2019.00232.
- Muglia, M., Seim, H., Taylor, P., 2020. Gulf stream marine hydrokinetic energy off Cape Hatteras, North Carolina. Mar. Technol. Soc. J. 54, 24 36. https://doi.org/10.4031/MTSJ.54.6.4.

NOAA (2022b). https://www.nhc.noaa.gov/.

 $NOAA~(2022a).~https://www.cpc.ncep.noaa.gov/products/precip/CWlink/daily_ao_index/teleconnections.shtml.\\$

Oliver, E.C.J., O Kane, T.J., Holbrook, N.J., 2015. Projected changes to Tasman Sea eddies in a future climate. J. Geophys. Res. 120, 7150 7165. https://doi.org/10.1002/2015JC010993.

Paerl, H., 2019. Recent increase in catastrophic tropical cyclone flooding in coastal North Carolina, USA: Long-term observations suggest a regime shift (and coauthors). Nat., Sci. Rep. 9, 10620. https://doi.org/10.1038/s41598-019-46928-9.

Palmen, E.H., Newton, C.W., 1969. Atmospheric Circulation Systems: Their Structure and Physical Interpretation, Vol. 13. Academic press.

Pinker, R., Bentamy, A., Katsaros, K., Ma, Y., Li, C., 2014. Estimates of net heat fluxes over the Atlantic Ocean. J. Geophys. Res. 119, 410 427. https://doi.org/10.1002/2013JC009386.

 $Pioneer\ Array\ Relocation\ (2023).\ https://oceanobservatories.org/pioneer-array-to-move-to-southern-mid-atlantic-bight-in-2024/.$

Reiter, E.R., 1963. Jet-Stream Meteorology. University of Chicago Press.

Rikus, L., 2015. A simple climatology of westerly jet streams in global reanalysis datasets part 1: mid-latitude upper tropospheric jets. Clim. Dyn. 50, 2285 2310. https://doi.org/10.1007/s00382-015-2560-y.

Rutgers (2023). https://marine.rutgers.edu/cool/sat data.

Sanders, F., 1988. Life history of mobile troughs in the upper westerlies. Mon. Weather Rev. 116, 2629 2648. https://doi.org/10.1175/1520-0493(1988)116% 3C2629;LHOMTI%3E2.0.CO;2.

Savidge, D., 2002. Wintertime shoreward near-surface currents south of Cape Hatteras. J. Geophys. Res. 107. https://doi.org/10.1029/2001JC001193.

Savidge, D., Austin, J., 2007. The hatteras front: august 2004 velocity and density structure. J. Geophys. Res. 112. https://doi.org/10.1029/2006JC003933.

Savidge, D., Bane, J., 2001. Wind and Gulf Stream influences on along-shelf transport and off-shelf export at Cape Hatteras, North Carolina. J. Geophys. Res. 106, 11505–11527. https://doi.org/10.1029/2000JC000574.

Schmitt, R., 2018. The ocean s role in climate. Oceanography 31, 32 40. https://doi.org/10.5670/oceanog.2018.225.

Schultz and co-authors, 2019. Extratropical cyclones: a century of research on meteorology s centerpiece. Meteorol. Monogr. https://doi.org/10.1175/AMSMONOGRAPHS-D-18-0015.1.

Schutt, M., Seim, H., 2020. Assessment of stability-based characterizations of North Carolina's offshore wind resource using a nested boundary layer method (https://doi.). J. Energy Power Technol. 2, 19. https://doi.org/10.21926/jept.2002006.

Seim, H., Savidge, D., Andres, M., Bane, J., Edwards, C., Gawarkiewicz, G., He, R., Todd, R., Muglia, M., Zambon, J., Han, L., Mao, S., 2022. An overview of the processes driving exchange at Cape Hatteras (PEACH) program. Oceanography. https://doi.org/10.5670/oceanog.2022.205.

Serreze, M., 1995. Climatological aspects of cyclone development and decay in the Arctic. Atmosphere-Ocean 33, 1 23.

Thomas, N., Seim, H., Haines, S., 2015. An observational, spatially explicit, stability-based estimate of the wind resource off the shore of North Carolina. J. Appl. Meteorol. Clim. 54, 2407 2425. https://doi.org/10.1175/JAMC-D-15-0090.1.

Todd, R., 2020. Export of middle atlantic bight shelf waters near Cape Hatteras from two years of underwater glider observations. e2019JC016006 J. Geophys. Res. 125. https://doi.org/10.1029/2019JC016006.

Wallace, J., Hobbs, P., 2006. Atmospheric Science: An Introductory Survey. ISBN 0-12-732951-X. Academic Press, p. 487. ISBN 0-12-732951-X.

Wallinga, J., Pettigrew, N., and Irish, J. (2003). The GoMOOS moored buoy design. Proceedings of the IEEE Oceans 2003 conference. 2596 2599. https://DOI: 10.1109/OCEANS.2003.178318.

Yang, H., Lohmann, G., Wei, W., Dima, M., Ionita, M., Liu, J., 2016. Intensification and poleward shift of subtropical western boundary currents in a warming climate. J. Geophys. Res. Oceans 121, 4928 4945. https://doi.org/10.1002/2015JC011513.

Yoder, J.A., Atkinson, L.P., Bishop, S.S., Hofmann, E.E., Lee, T.N., 1983. Effect of upwelling on phytoplankton productivity of the outer southeastern United States continental shelf. Cont. Shelf Res. 1, 385 404. https://doi.org/10.1016/0278-4343(83)90004-3.

Zambon, J.B., He, R., Warner, J.C., Hegermiller, C.A., 2021. Impact of SST and surface waves on Hurricane Florence (2018): a coupled modeling investigation. Weather Forecast. 36, 1713 1734. https://doi.org/10.1175/WAF-D-20-0171.1.